Defense Threat Reduction Agency
8725 John J. Kingman Road, MS 6201
Fort Belvoir, VA 22060-6201

DTRA-TR-02-13

TECHNICAL REPORT

Station Calibration and Regionalization in China and Surrounding Areas

January 2005

DTRA 01-99-C-0016

Thomas Hearn
James Ni

Prepared by:
New Mexico State University
Physics Department, 3D
Gardiner Hall
Las Cruces, NM 88003

DESTRUCTION NOTICE:

Destroy this report when it is no longer needed.
Do not return to sender.

PLEASE NOTIFY THE DEFENSE THREAT REDUCTION AGENCY, ATTN: BDMI, 8725 JOHN J. KINGMAN ROAD, MS-6201, FT BELVOIR, VA 22060-6201, IF YOUR ADDRESS IS INCORRECT, IF YOU WISH IT DELETED FROM THE DISTRIBUTION LIST, OR IF THE ADDRESSEE IS NO LONGER EMPLOYED BY YOUR ORGANIZATION.

DISTRIBUTION LIST UPDATE

This mailer is provided to enable DTRA to maintain current distribution lists for reports. (We would appreciate you providing the requested information.)

- ❑ Add the individual listed to your distribution list.
- ❑ Delete the cited organization/individual.
- ❑ Change of address.

Note:
Please return the mailing label from the document so that any additions, changes, corrections or deletions can be made easily. For distribution cancellation or more information call DTRA/BDMI (703) 767-4724.

NAME: _____

ORGANIZATION: _____

OLD ADDRESS	NEW ADDRESS
_____	_____
_____	_____
_____	_____

TELEPHONE NUMBER: ( ) _____

DTRA PUBLICATION NUMBER/TITLE	CHANGES/DELETIONS/ADDITONS, etc. *(Attach Sheet if more Space is Required)*
_____	_____
_____	_____
_____	_____

DTRA or other GOVERNMENT CONTRACT NUMBER: _____

CERTIFICATION of NEED-TO-KNOW BY GOVERNMENT SPONSOR (if other than DTRA):

SPONSORING ORGANIZATION: _____

CONTRACTING OFFICER or REPRESENTATIVE: _____

SIGNATURE: _____

DEFENSE THREAT REDUCTION AGENCY
ATTN: BDMI
8725 John J. Kingman Road, MS-6201
Ft Belvoir, VA 22060-6201

DEFENSE THREAT REDUCTION AGENCY
ATTN: BDMI
8725 John J. Kingman Road, MS-6201
Ft Belvoir, VA 22060-6201

REPORT DOCUMENTATION PAGE

Form Approved

1. AGENCY USE ONLY *(Leave blank)*	2. REPORT DATE	3. REPORT TYPE AND DATES COVERED
	050100	Technical 990201 - 020131

4. TITLE AND SUBTITLE

Station Calibration and Regionalization in China and Surrounding Areas

5. FUNDING NUMBERS

C – DTRA01-99-C-0016
PE – 99Q
PR – CD
TA – CD
WU – DH 66422

6. AUTHOR(S) Thomas Hearn and James Ni

7. PERFORMING ORGANIZATION NAME(S) AND ADDRESS(ES)

New Mexico State University
Physics Department , 3D
Gardiner Hall
Las Cruces, NM 88003

8. PERFORMING ORGANIZATION REPORT NUMBER

9. SPONSORING/MONITORING AGENCY NAME(S) AND ADDRESS(ES)

Defense Threat Reduction Agency
8725 John J. Kingman Road, STOP-6201
Fort Belvoir, VA 22060-6201

TDCN/Barber

10. SPONSORING/MONITORING AGENCY REPORT NUMBER

DTRA-TR-02-13

11. SUPPLEMENTARY NOTES

This work was sponsored by the Defense Threat Reduction Agency under RDT&E RMC Code B 4613 D CD CD 66422 5P50 A 25904D.

12a. DISTRIBUTION/AVAILABILITY STATEMENT

Approved for public release; distribution is unlimited.

12b. DISTRIBUTION CODE

13. ABSTRACT *(Maximum 200 words)*

NMSU seismologist, in conjunction with seismologist from the Institute of Geophysics of the China Seismological Bureau (IG/CSB), have collected seismic data to calibrate International Monitoring System stations in China and document propagation characteristics of regional phases in China. Much of the work is focused on the Annual Bulletin of Chinese Earthquakes. We obtained copies of these bulletins for 1983-1995. A tomographic image of Pn velocity beneath China was made and regional travel-time curves for CSDN and IMS stations were produced. Locations from the bulletin were compared with those obtained by the Preliminary International Data Center fro 1995.

Seismograms from CDSN stations in China and from temporary PASSCAL experiments were collected to examine the regional phase characteristics of Sn and Lg phase propagation. Sn waves propagate only in cratonic regions of China and southern Tibet where Indian Shield under thrusts it. Lg propagates efficiently throughout most eastern and northern China but is highly attenuated within the Tibetan Plateau. We used regional waveform data collected from three broadband PASSCAL experiment in Tibet to estimate Lg Q values. We found Lg Qo= 100-120 in central Tibet and Lg Qo= 60-70 in the southernmost Tibet.

14. SUBJECT TERMS		15. NUMBER OF PAGES
Seismology	Tomography	73
China	Station Calibration	16. PRICE CODE

17. SECURITY CLASSIFICATION OF REPORT	18. SECURITY CLASSIFICATION OF THIS PAGE	19. SECURITY CLASSIFICATION OF ABSTRACT	20. LIMITATION OF ABSTRACT
UNCLASSIFIED	UNCLASSIFIED	UNCLASSIFIED	SAR

CONVERSION TABLE

Conversion Factors for U.S. Customary to metric (SI) units of measurement.

MULTIPLY →	BY →	TO GET
TO GET ←	BY ←	DIVIDE

angstrom	1.000 000 X E -10	meters (m)
atmosphere (normal)	1.013 25 X E +2	kilo pascal (kPa)
bar	1.000 000 X E +2	kilo pascal (kPa)
barn	1.000 000 X E -28	meter^2 (m^2)
British thermal unit (thermochemical)	1.054 350 X E +3	joule (J)
calorie (thermochemical)	4.184 000	joule (J)
cal (thermochemical)/cm^2	4.184 000 X E -2	mega joule/m^2 (MJ/m2)
curie	3.700 000 X E -1	*giga becquerel (GBq)
degree (angle)	1.745 000 X E -2	radian (rad)
degree Fahrenheit	tr=(t°f + 459.67)/1.8	degree kelvin (K)
electron volt	1.602 19 X E -19	joule (J)
erg	1.000 000 X E -7	joule (J)
erg/second	1.000 000 X E -7	watt (W)
foot	3.048 000 X E - I	meter (m)
foot-pound-force	1.355 818	joule (J)
gallon (U S liquid)	3.785 412 X E -3	meter^3 (m^3)
inch	2.540 000 X E -2	meter (m)
jerk	1.000 000 X E +9	joule (J)
joule/kilogram (J/kg) radiation dose absorbed	1.000 000	Gray (GY)
kilotons	4.183	terajoules
kip (1000 Ibf)	4.448 222 X E +3	newton (N)
kip/inch^2 (ksi)	6.894 757 X E +3	kilo pascal (kPa)
ktap	1.000 000 X E +2	newton-second/m^2 (N-s/m^2)
micron	1.000 000 X E -6	meter (m)
mi I	2.540 000 X E -5	meter (m)
mile(intemational)	1.609 344 X E +3	meter (m)
ounce	4.448 222	kilogram (kg)
pound-force (Ibs avoirdupois)	1.751 268 X E +2	newton (N)
pound-force inch	6.894 757	newton-meter (N*m)
pound-force/inch	2.834 952 X E -2	newtodmeter (Nlm)
pound-force/foot^2	1.129 848 X E - 1	kilo pascal (kPa)
pound-force/inch^2 (psi)	4.788 026 X E -2	kilo pascal (kPa)
pound-mass (Ibm avoirdupois)	4.535 924 X E - 1	kilogram (kg)
pound-force/foot^2 (moment of inertia)	4.214 011 X E -2	kilogram-meter^2 (kg*m^2)
pound-mass/foot^3	1.601 846 X E + I	kilogram-meter^3 (kg*m^3)
rad (radiation dose absorbed)	1.000 000 X E -2	**Gray(Gy)
roentgen	2.579 760 X E -4	coulomb/kilogram (C/kg)
shake	1.000 000 X E -8	second (s)
slug	1.459 390 X E + I	kilogram (kg)
torr (mm HG. 0°C)	1.333 22 X E -1	kilo pascal (kPa)

*The bacquerel (Bq) is the SI unit of radioactivity; 1 Bq = 1 event/s.

**The Gray (GY) is the SI unit of absorbed radiation.

TABLE OF CONTENTS

FIGURES

TABLES

SECTION 2

DATA COLLECTION

Our data set of the Annual Bulletin of Chinese Earthquakes (ABCE) consists of both paper bulletins and digital data sets provided by our colleagues from the China Seismological Bureau (CSB). These data are from over 110 stations of the Chinese national network (Figure 2-1). The seismometers are mostly short-period (~1 Hz) recording on paper. Long-period instruments with periods of around 10 s are usually co-located with the short-period instruments. These were used for magnitude measurements.

We obtained paper copies of the ABCE spanning 1983 to 1995 and digital versions of the 1991 to 1995 bulletins. The digital data contain the same locations and information as the paper bulletins but often include readings at international stations that were collected by the International Seismological Centre. We had data from the 1984 to 1989 bulletins transcribed into digital form. This yields over ten years of digital data.

We also collected paper copies of the Bulletin of Seismological Observations of Chinese Stations (BSOCS) for 1979, 1992, and 1993. These bulletins are a teleseismic version of the ABCE. They contain mostly readings from about 25 Chinese stations that traditionally report to the International Seismological Centre. Most of the readings are teleseismic, but local events are also included. Event locations are either from the ABCE or the ISC.

The data quality from the ABCE is exceptional. Seismic stations in China have routinely identified and picked all seismic phases both regional and teleseismic for events in and around China and used them for event location. These phases include Pg, Pn, P, PP, pP, Sg, Sn, S, SS, sS, sP, PcP, S11, ScS, P11, ScP, and PcS (Figure 2-2). Regional Pg, Pn, Sg, and Sn phases were identified up to nine degrees distance, after which they were classified as S or P. In addition to travel-time picks and locations, the amplitude and period measurements needed for mb, mB, and Ms magnitude estimates were also routinely reported by the ABCE. Amplitude measurements were routinely made at the majority of stations. The quantity and thoroughness of these bulletin data make this the best such data set in the world.

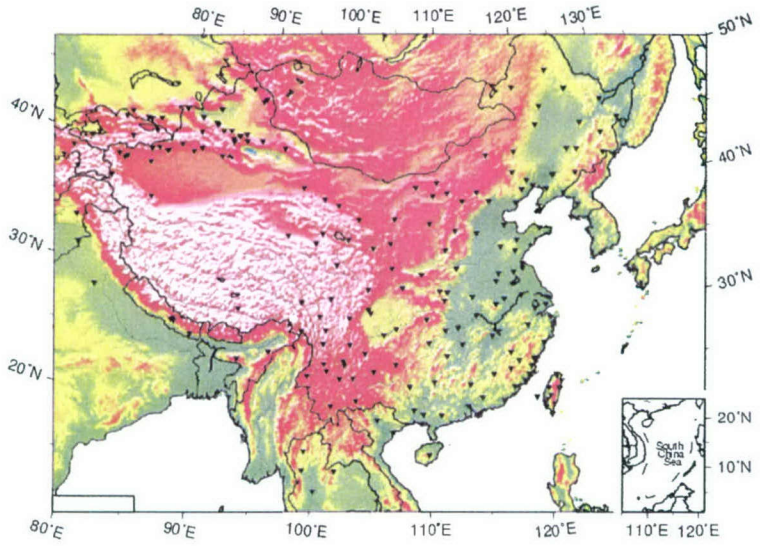

Figure 2-1. Shaded topography of China showing locations of regional seismic stations used in the Annual Bulletin of Chinese Earthquakes.

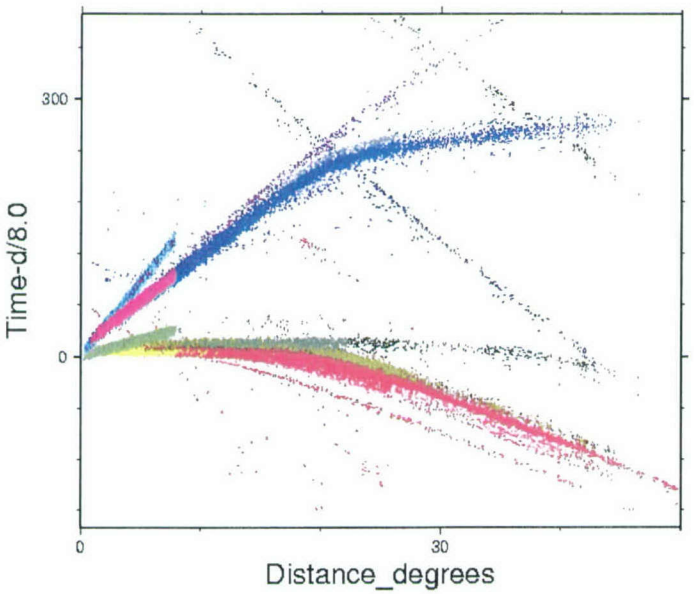

Figure 2-2. P-wave first arrival travel times from the Chinese bulletins (ABCE) for 1991 through 1995. Pg, Pn and a distant P branch are clearly visible. The ABCE routinely identifies arrivals as Pg, Pn, P, PP, pP, Sg, Sn, S, SS, sS, sP, PcP, S11, ScS, P11, ScP, and PcS.

SECTION 3

PN TOMOGRAPHY BENEATH CHINA

3.1 INTRODUCTION.

We have applied the Pn tomography algorithm of Hearn (1999) to Pn data from the ABCE to image the P-wave velocity and anisotropy at the surface of the mantle. Raypaths for these data cover most of central and Eastern China. Tibet and Western China have scant, but useable coverage. We used raypaths between 1.8 and 15 degrees distance and only stations and events with more than 9 arrivals at them. The final Pn data set used contains over 50,000 arrivals that span most of China (Figure 3-1).

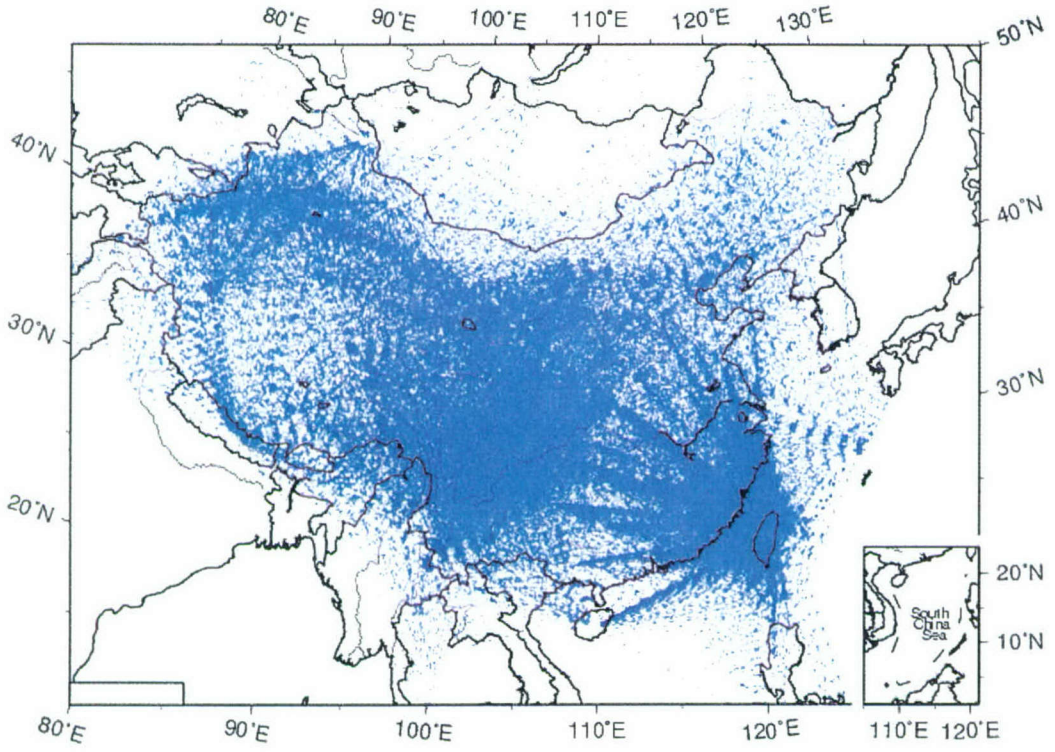

Figure 3-1. Pn raypaths used in the tomography. Distances were restricted to 1.8 to 15 degrees. About 50,000 raypaths are shown.

3.2 REGULARIZATION METHOD AND PN ANISOTROPY.

Tomography problems are always regularized in some manner. We have chosen to use Laplacian damping, but there are many viable methods. The damping parameter trades-off the image noise-level with image resolution. When damping is too low, the resolution is good but overwhelmed by the noise; when damping is too high there is little noise but the resolution width is too large to be useful. Between these two damping extremes is an optimal level that balances noise and resolution. When there is only one damping parameter in the problem the damping level can be set by visually inspecting the results as is usually done with seismic tomography. However, when multiple damping parameters are present visual inspection becomes too subjective to be of use and other criteria must be used. In this paper, we are particularly interested in the relative amount of anisotropy that is needed in the solution and use the information criteria to resolve the issue.

The Akaike Information Criteria (AIC) was first introduced to determine the optimal model order for regression problems in statistics (Akaike, 1973; McQuarrie and Tsai, 1998). It also has several cousins such as the corrected-AIC (AICc), Bayesian Information Criteria, Mallows Cp-criteria, and the Swartz Information Criteria (SIC). These criteria have been extended to damped-least squares type problems. From a practical viewpoint, they are used to determine the damping constants. We use it to determine the appropriate levels of the velocity and anisotropy variations in the seismic tomography. From a theoretical viewpoint, however, the information criteria produce solutions that have optimal prediction capability.

In this study we present results using the SIC. It, like the AIC, is implemented as a norm to be minimized. For the SIC

$$SIC = \log(SOS / n) + \log(n) * k / n$$

where SOS is the sum of the squared residuals of the inversion, n is the total number of data, and k is the effective number of parameters of the inversion (McQuarrie and Tsai, 1998). Both SOS and k are functions of the damping parameters in the inversion. The first term of the SIC is the logarithm of the variance of the damped least squares inversion. This term decreases with increasing damping. The second term is a penalty term that decreases with increasing damping. It penalizes the solution for having too many free parameters. Determining the minimum SIC is easily accomplished by running repeated damped least-squares inversions for different damping parameters and estimating the SIC for each inversion. The optimal damping parameters produce the minimum SIC.

The most difficult part of applying information criteria techniques to large tomographic inversions is determining the number of effective parameters. For damped type inversions, the trace of the resolution matrix gives an approximate estimate of the number of effective parameters. However, the LSQR conjugate-gradient method used in this study does not produce the resolution matrix directly. We therefore use the following approximation for the trace of the resolution matrix:

$$k = \text{trace}\left((G^T G + D^T D)^{-1} G^T G \right) \approx \text{trace}\left(G^T G \left(\text{diag}\,(G^T G + D^T D)\right)^{-1} \right)$$

where G is the design matrix and D is the damping matrix. This approximation meets the need of being easily computed while monotonically varying between the total number of parameters and zero with increasing damping.

To choose the appropriate information norm, we tested several of them. The AIC, AICc, FPE, HQ, and Cp norms were found to substantially underdamp the solutions while the SIC seemed to slightly overdamp. This is perhaps because the SIC was developed using a Bayesian criteria that is more appropriate for large regression problems. A similar Bayesian measure, the BIC, could not be tested the conjugate-gradient inversion algorithm we use cannot compute the necessary determinants.

In our study, the most important factor was that the SIC gave an objective measure for setting the damping parameters for both the velocity and anisotropy perturbations. This is particularly important for determining the relative amount of anisotropy needed by the solution.

We used the minimum SIC to determine a damping level of 650 for the velocity parameters when no anisotropy was allowed in the inversion (Figure 3-2). At this damping level, the standard error is 1.03 s; the rms level of velocity perturbations is 0.080 km/s with a maximum perturbation of 0.38km/s. When anisotropy was included in the inversion found the SIC determined damping parameters were 950 and 650 for the velocity and anisotropy, respectively (Figure 3-3). The resulting inversion had an estimated standard error of 1.07 s; the rms velocity variation is .047 with a maximum of 0.25 km/s; the average anisotropy variation is .009 km/s but with a maximum of 0.46 km/s. Bootstrap estimates of all parameter errors found them to be very small.

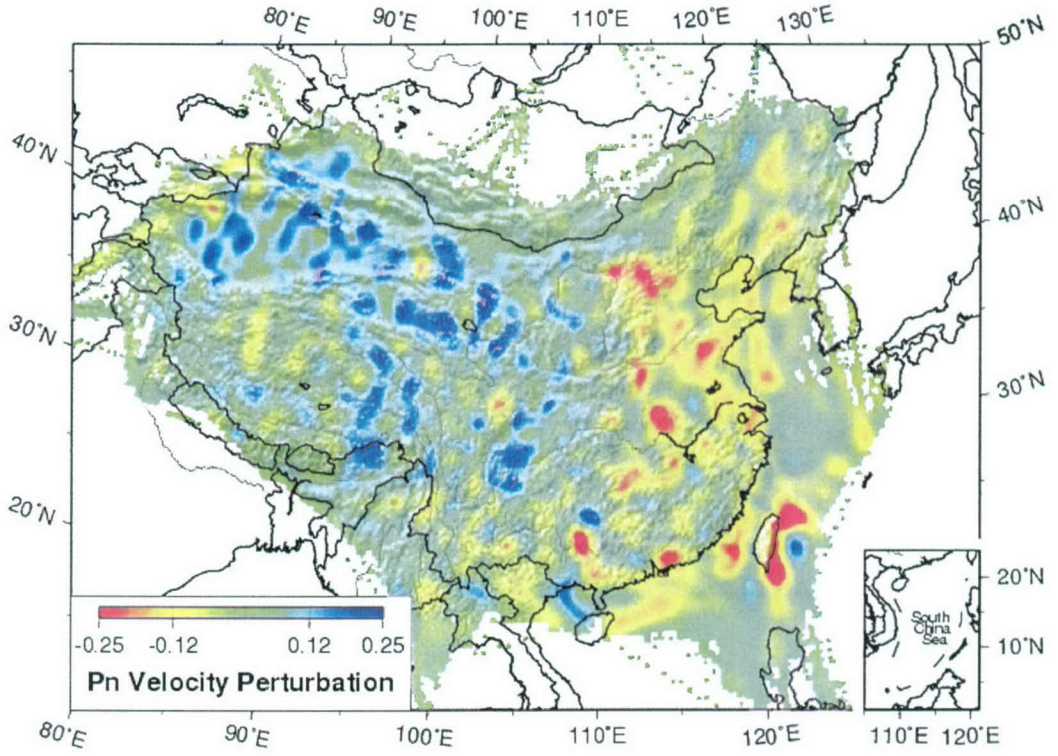

Figure 3-2. Isotropic tomography results showing velocity perturbations (in km/s) relative to a mean velocity of 8.0 km/s. The damping level determined by the SIC is set at 650.

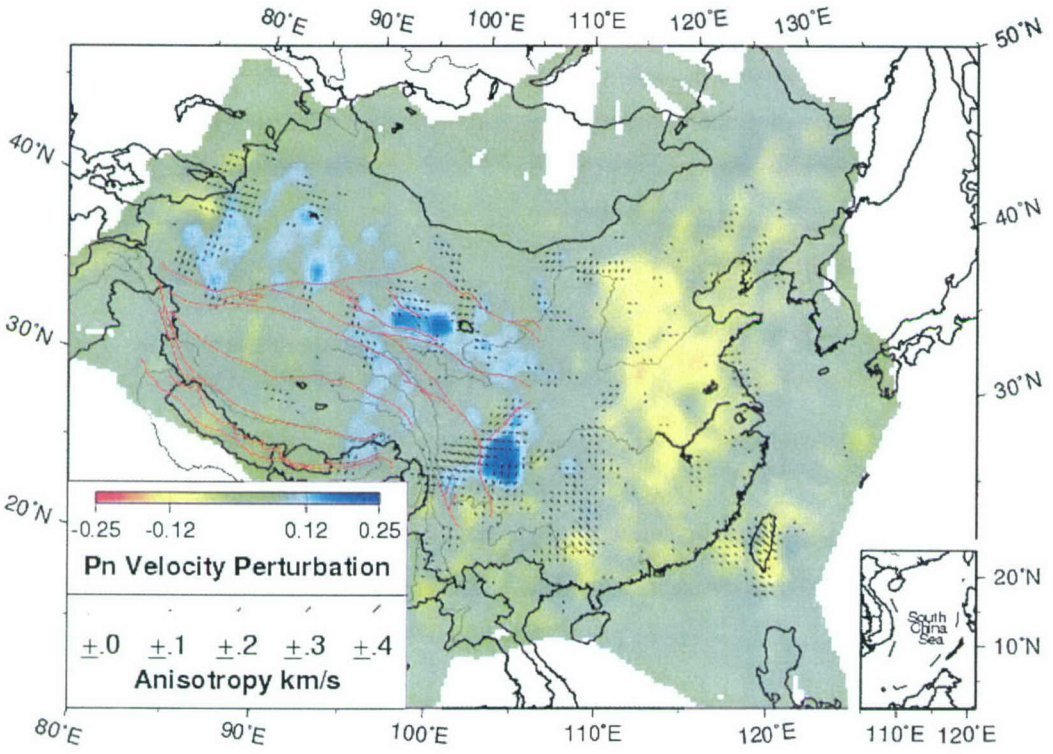

Figure 3-3. Anisotropic tomography results showing velocity and anisotropy perturbations (in km/s) relative to a mean velocity of 8.0 km/s. Much of the travel-time data has been projected into the anisotropic component. Damping levels were set using the SIC at 950 and 650 for the velocity and anisotropy components, respectively.

The low level of anisotropy found for most of China makes it difficult to interpret. Most of the anisotropy is concentrated around Taiwan and in Sichuan province, but results near Taiwan may be heavily biased by poor locations and depth estimates. An anisotropic checkerboard test (Figure 3-4) indicates that there is a substantial amount of velocity-anisotropy trade-off at the chosen damping levels. Specifically, sharp variations in velocity map into anisotropy. These observations suggest that much of the imaged anisotropy is the result of sharp variations in velocity. When this same anisotropic checkerboard dataset was imaged without anisotropy, the results were much better (Figure 3-5). Statistically, the no-anisotropy model has a lower rms error than the model that includes anisotropy. This again suggests that the anisotropy, despite the fact that it fits the data with fewer effective parameters, is unnecessary. The model without anisotropy is our preferred model.

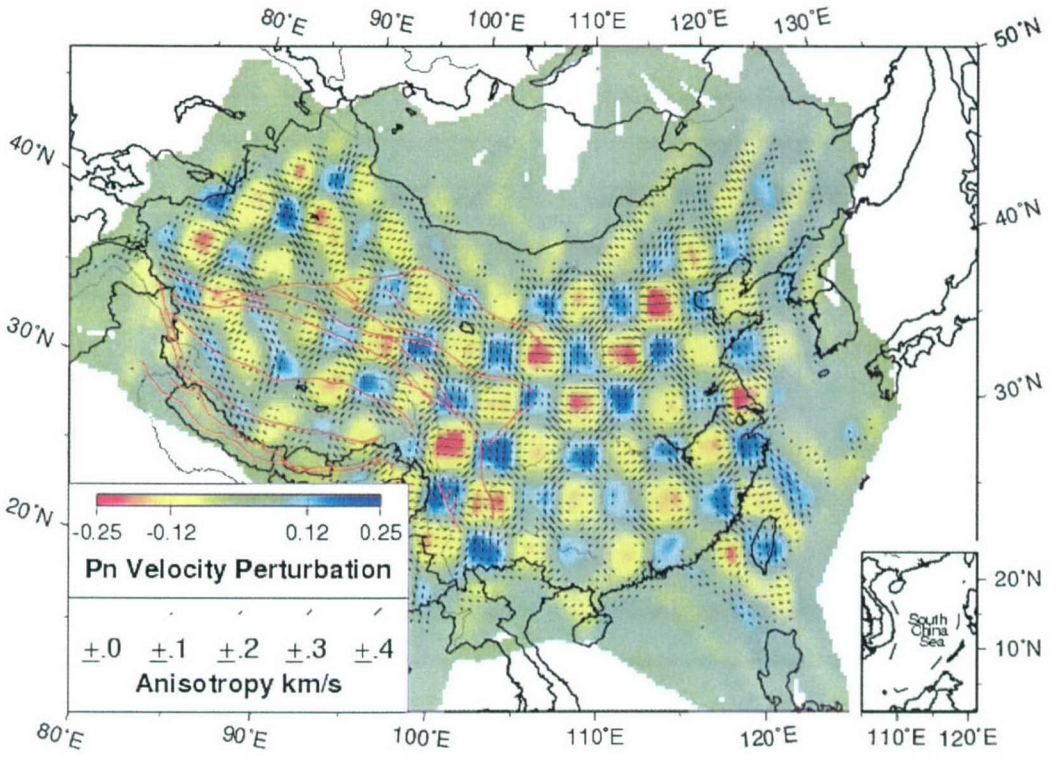

Figure 3-4. Checkerboard test of anisotropic tomography for the SIC determined damping parameters. The original image included both anisotropy and velocity variations as squares of alternating high and low velocity with alternating east-west and north-south anisotropy. The test used three-by-three degree squares. Much of the imaged anisotropy has diagonal northeast or southeast directions. This results from the velocity anomaly trade-off with the anisotropy. The figure shows velocity and anisotropy perturbations (in km/s) relative to a mean velocity of 8.0 km/s.

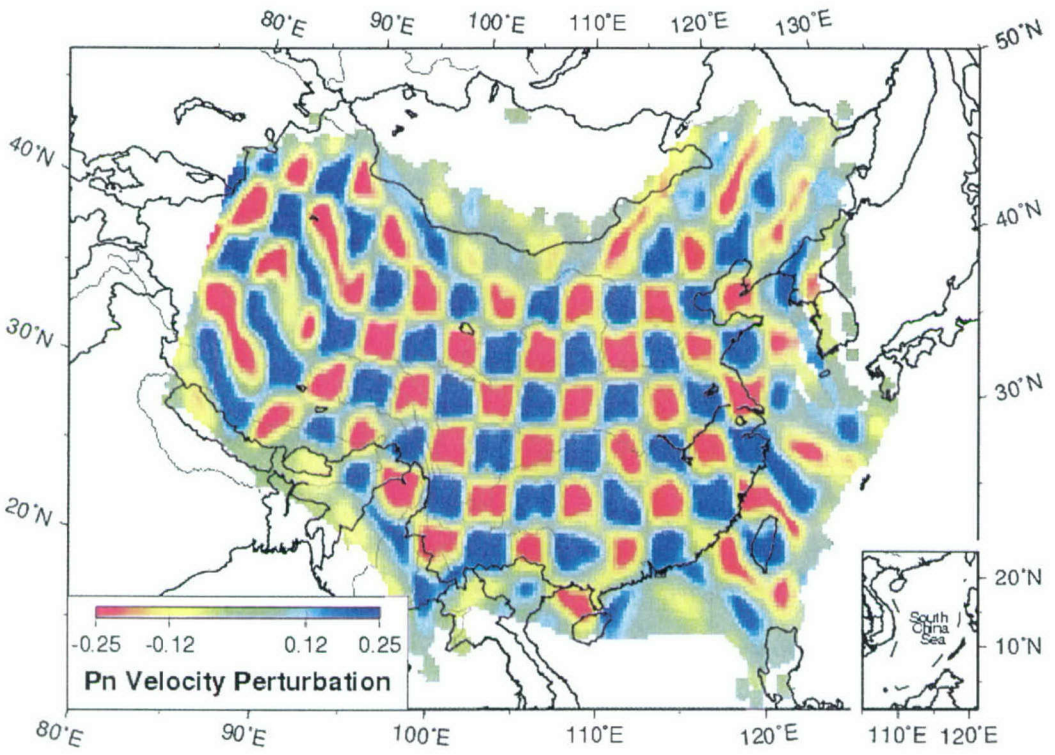

Figure 3-5. Checkerboard test for tomography with no anisotropy but with anisotropy in the original checkerboard test data. This test used three-by-three degree squares. Other tests showed that features as small as one-by-one degree could be imaged in east-central china. The figure shows velocity perturbations (in km/s) relative to a mean velocity of 8.0 km/s.

3.3 DISTANCE DEPENDENCE OF THE RESULTS.

Lithospheric structure may vary from top to bottom. The rays used in this study all travel through the lithosphere; rays that dive into the asthenosphere have higher apparent velocities, and are not seen as first arrivals until around 20 degrees distance. Shorter raypaths sample only the top of the lithosphere while more distant rays sample close to the base of the lithosphere. To investigate how important an effect this is, the data were divided into two halves of nearly equal sizes and inverted tomographically. Shorter raypaths, between 1.8 and 9.5 degrees, sample the upper-lithosphere. Longer raypaths, between 9.5 and 15 degrees penetrate the top of the upper lithosphere but are mostly in the lower lithosphere. Comparison of the two inversions gives insight into the how the Chinese lithosphere varies with depth.

The upper-lithosphere inversion using the shorter raypaths is shown in Figure 3-6. The mean Pn velocity for these data was 8.01 km/s. Western China could not be imaged because the station spacing was too sparse. The image is similar to that of the full data set. The long-raypath

inversion (Figure 3-7) gives a similar, but different image than the short-raypath inversion. The mean Pn velocity was 8.17 km/s for these long rays suggesting that the average mantle velocity varies by about 0.2 km/s from the top to the bottom of the lithosphere at 80-200 km depth.

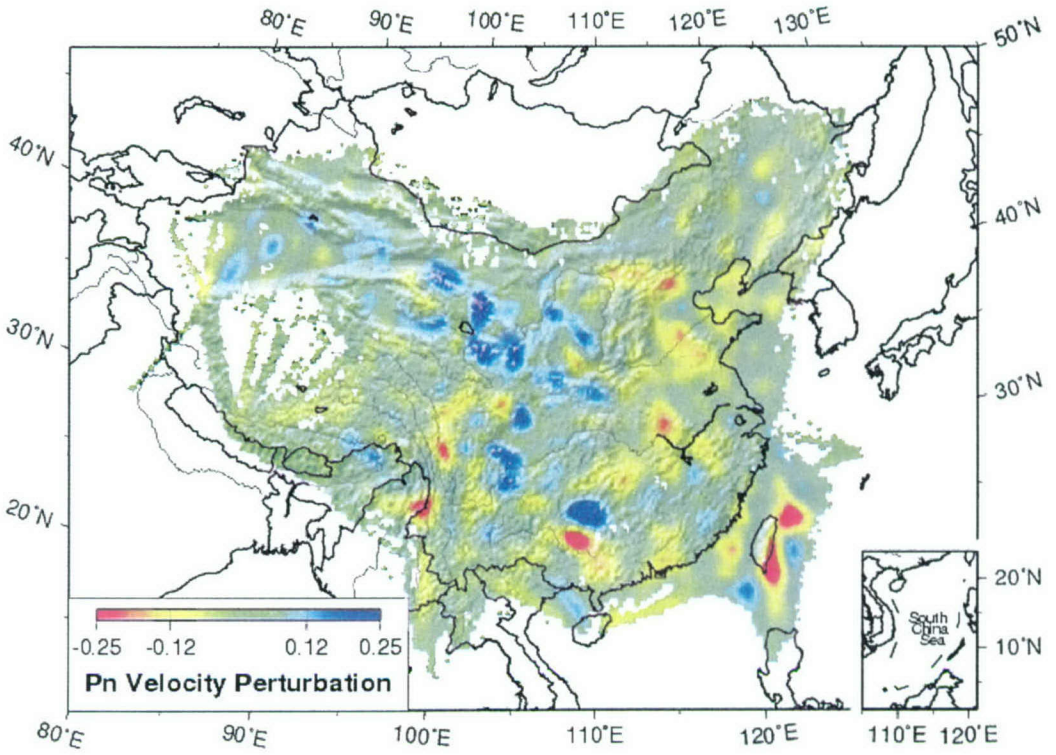

Figure 3-6. Inversion of short raypaths (1.8 to 9.5 degrees distance). The figure shows velocity perturbations (in km/s) relative to a mean velocity of 8.0 km/s.

The short-raypath and long-raypath inversions can be interpreted as imaging the upper and lower lithosphere. Similarities show features that extend throughout the lithosphere and differences show features that are predominantly within the upper- or lower-lithosphere. The major velocity patterns of the two inversions are quite similar. In both images, Western China has higher velocities than in the east. Sichuan Basin is a prominent high velocity region that is in both images; the northeastern corner of Tibet in Qinghai province is similar. This suggests that these regions have deep lithospheric roots and may serve as buttresses to the northern and eastern expansion of Tibet. Differences between the two images are of interest. The rifting in Eastern China is much more pronounced in the long-raypath image, suggesting that these features are seated in the deeper lithosphere and are driven from the asthenosphere below. Low velocities beneath Northern Tibet are also prominent for the long raypaths, but there was insufficient short-raypath data in the area for a comparison. There are several regions of low-velocity along the eastern margin of Tibet in the short-raypath images that are not in the long-raypath image. These

correspond to extension along the Panxi rift and Xiaojiang fault system. The implied shallowness of these low-velocity zones suggests that the rifting occurs primarily in the upper lithosphere is not driven by asthenospheric processes. Rather, it is driven by the oblique extension of Southeast Asia moving away from Tibet (Royden and Burchfiel, 1997; Chen et. al., 2000).

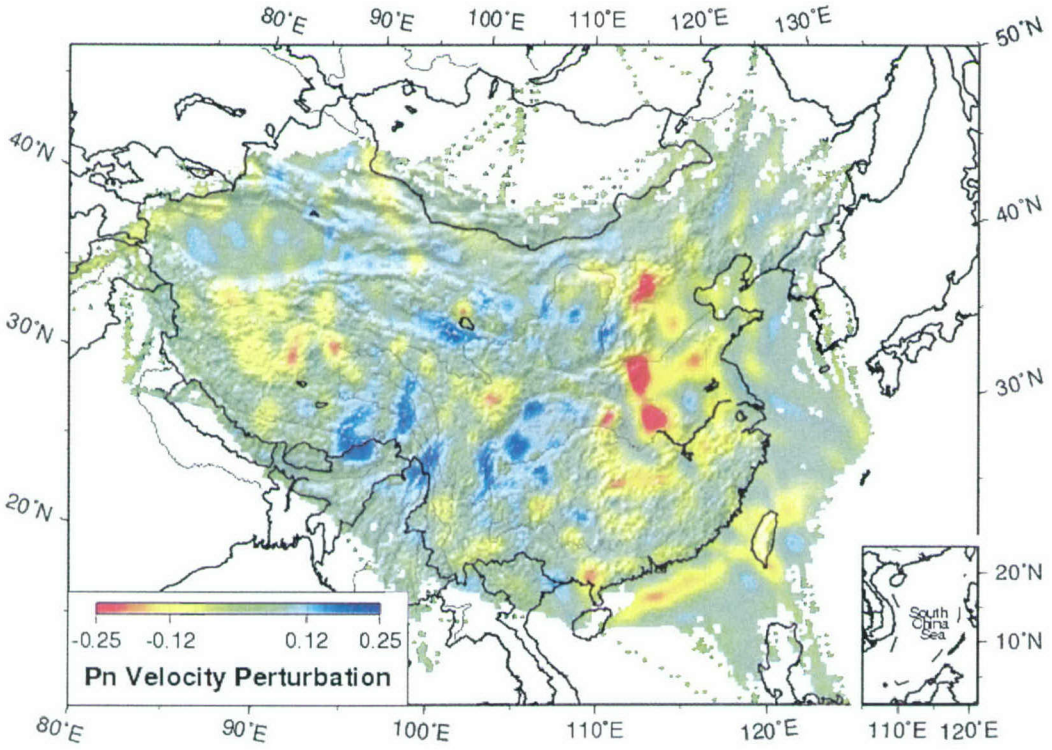

Figure 3-7. Inversion of long raypaths (9.5 to 15 degrees distance). The figure shows velocity perturbations (in km/s) relative to a mean velocity of 8.0 km/s.

3.4 TECTONIC INTERPRETATION.

The inversion yields an average Pn velocity of 8.05 km/s for all of China consistent with the worldwide average of 8.09 km/s (Christensen and Mooney, 1995). The key results are presented as Figures 3-8, 3-9 and 3-10. Figure 3-8 shows the regionally varying Pn velocities superimposed upon the topography. Figures 3-9 and 3-10 are the station delays and the event delays. Both station and event delays represent the combined effect of crustal velocity and thickness. Event delays, however, absorb any systematic errors in origin time or depth in the event location. In most Pn tomography studies (e.g. Hearn, 1999], the origin-time and depth

parameters are poorly determined and this creates such scatter in the event delays that they are uninterpretable. This is not the case for the ABCE data, and it indicates that events in China are exceptionally well located.

The station delays can be interpreted as a rough map of crustal thickness in China. For a constant velocity crust, 1 second of delay time represents approximately 10 km of crustal thickening. Late station and event delays in Tibet then imply that the crust there is 30 to 40 km thicker than the crust in Eastern China. Events north of the Tarim Basin and in the Tien Shan also show late delays indicating crust that is 10 to 20 km thicker than Eastern China. A thin crust is also apparent southeast of Tibet where extension is occurring.

The high Pn velocity regions are stable cratonic areas – Junggar Basin, Tarim Basin, Taidam Basin and Sichuan Basin. These cratonic areas were not greatly affected by tectonic and magmatic activity since its formation and hence there is lower temperature in the mantle lid and higher Pn velocity. These shield regions must also be regions of strong lithosphere. Their higher density mantle may have aided in the development of these basins. Pn velocity beneath Tibet decreases from south to north as has been found in previous Tibet studies (Ni and Barazangi, 1983, 1984; McNamara, 1997). This suggests that the subducted Indian plate ends somewhere beneath central Tibet. Eastern China has much lower Pn velocities. Along the Southeastern Tibet margin, low Pn velocities are found suggesting that high temperatures and possible partial melt exists in the mantle there.

Variation in Pn velocity within the Tibetan Plateau has been previously observed. Southern Tibet has a high Pn velocity and is probably underlain by the under-thrusting Indian continental lithosphere (Barazangi and Ni, 1983; Ni and Barazangi, 1984; Beghoul et al., 1993; Nelson et al., 1996; Huang et al., 2000). Our data in Tibet, with limited ray coverage, barely resolve the Pn velocity between Northern and Southern Tibet. In Northern Tibet, the Pn velocity is about 7.9 km/s (also see McNamara et al., 1997). The relatively low velocity in Northern Tibet has been interpreted as thermally weakened Asian mantle lid that is being squeezed between the advancing Indian lithosphere to the south and similarly rigid Tsaidam and Tarim lithosphere to the north and west (Huang et al., 2000). Our results show that the relatively inactive Sichuan Basin is underlain by a deep high-velocity lithospheric root. It is moving away from Tibet along with the South China Block. The Tarim Basin and the Qinghai Shan mountains also show a deep high-velocity lithosphere, but these are areas where Tibet is actively extending (Tapponnier, 2001). This high velocity mantle may have subducted beneath Tibet from the north.

Beneath regions adjacent to the southeastern edge of the Tibetan plateau where coverage is good, we found low Pn velocity (<7.8 km/s) regions in the upper lithosphere that do not extend to the base of the lithosphere. These regions correspond to magmatic (extensive Quaternary basalt) and tectonic activity in the Panxi rift and Xiaojiang fault system. The tendency of NNE alignment of the Panxi rift suggests an orientation controlled by the simple shearing motion in the Asian lithosphere. Such an interpretation is consistent with that the observation that Panxi rift and Xiaojiang pull-apart lie in a trans-extensional tectonic environment produced by the shearing between India and Asia plate, which is currently taking place on a transform boundary along the right-lateral Sagaing fault (Guzmann-Spazelie and Ni, 1993). These forces originate from the plate motions and takes place passively without any asthenospheric contribution.

Eastern China is comprised of the Archean North China block and South China block. These cratonic blocks collided first during the late Permian. After the collision, it experienced widespread tectonothermal reactivation events during Late Mesozoic and Cenozoic, as indicated by emplacement of voluminous late Mesozoic granites and extensive Cenozoic volcanism associated with subduction of Pacific and Philippine plates (Yin and Nie, 1996). These tectonothermal events resulted in replacement of the old, cold, thick, and depleted lithospheric mantle by young, hot, thin, and fertile lithospheric mantle accompanied by lithospheric thinning. Widespread Cenozoic rifting and associated alkaline basalt in the North China block is well documented. GPS measurements indicate that the South China block is moving southeastward at ~10 mm/year while the North China block is moving eastward at ~ 5 mm/year (Chen et al., 2000; Michel et al., 2000; Holt et al., 2000). The faster motion of the South China block produces extension within the North China block.

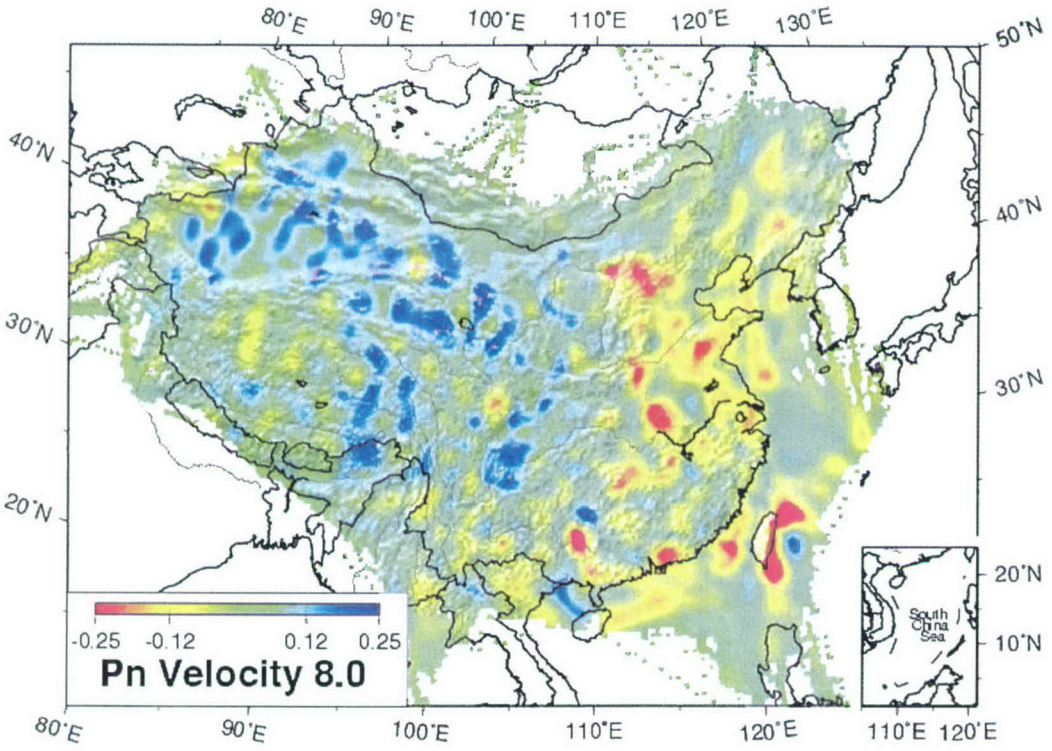

Figure 3-8. Final model of Pn velocities beneath China. This figure was constructed with raypaths between 1.8 and 15 degrees distance, nine arrivals minimum per station and event, and a damping factor of 650. The figure shows velocity perturbations (in km/s) relative to a mean velocity of 8.0 km/s.

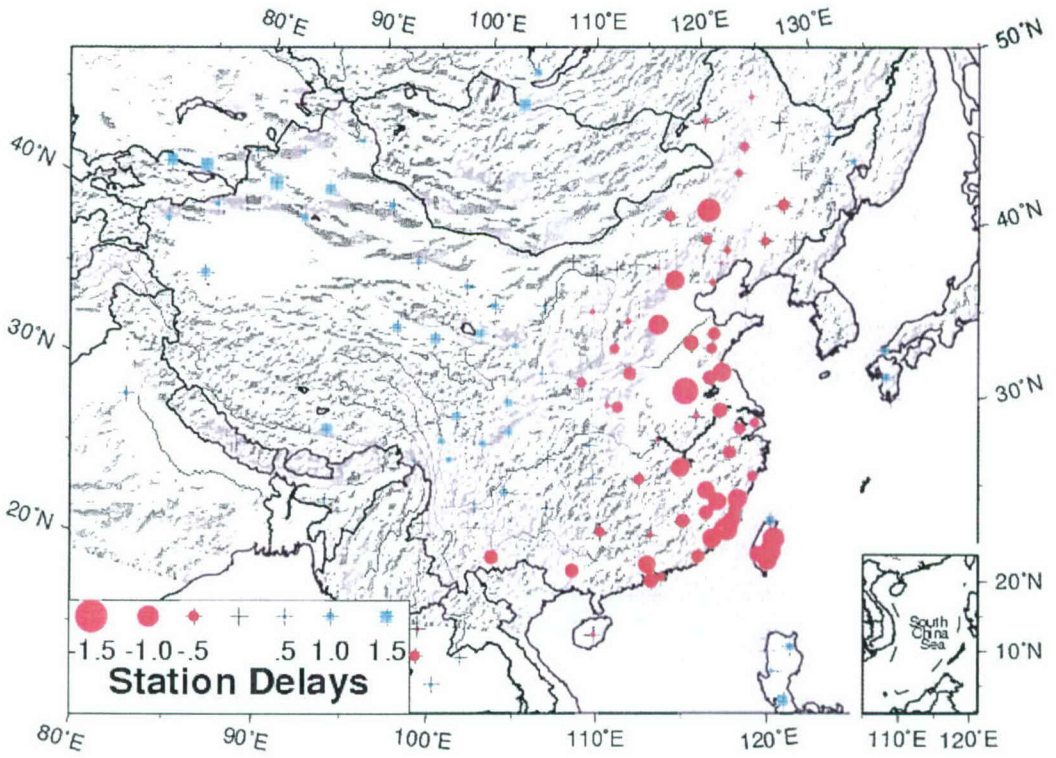

Figure 3-9. Final model of Pn station delays beneath China. Each second of relative travel-time delay corresponds to approximately 10 km of crustal thickness change.

The Pn velocity image shows that low-velocity structures are NNE-elongate and correspond to pattern of young volcanism and regions of large extension. Furthermore, the low-velocities are more apparent in the bottom of the lithosphere suggesting that asthenospheric processes have created zones of partial melt above them. The Shanxi rift, a continental rift located on the eastern edge of the Ordos Plateau is characterized with a very low Pn velocity that mimics the en-echelon pattern of the right stepping Shanxi grabens. Beneath the Tai Shan, where the Tan Lu fault crosses, a very pronounced Pn velocity zone was imaged. The high elevation of this mountain region must be partially supported by the buoyant mantle, a feature that was not known before this study. The Hannuoba alkaline basalt that occurs north of Beijing and extends into Inner Mongolia is underlain by low Pn-velocity. The overall low Pn velocity pattern and correlation with magmatism clearly demonstrate that the lithospheric mantle beneath the North China block is hot and partially melted. This interpretation is also consistent with the observed inefficient Sn propagation in this region (Rapine and Ni, 2002). The low-velocities of the North China Block are more apparent in the deeper lithosphere (Figure 3-7).

The interior of the North China block consists of the elevated Ordos platform and the Yin Chuan rift located east of the Ordos platform. Pn velocities beneath these regions are normal and indicate that Yin Chuan rift is a structural rift in an early stage of rifting. The thick crust there supports the Ordos platform.

The eastern part of South China block was a magmatic arc during much of the Mesozoic to Cenozoic. Low Pn velocity regions correlate well with regions of Cenozoic magmatism. The ray coverage near Taiwan is poor and thus imaged features are not reliable. A very low velocity feature is found north of Hainan Island in the Guangdong province, particularly when only the long-raypath data is used. The close proximity of this feature to the Red River fault and South China Sea suggest a possible relationship between the opening of the South China Sea and the low Pn velocity feature.

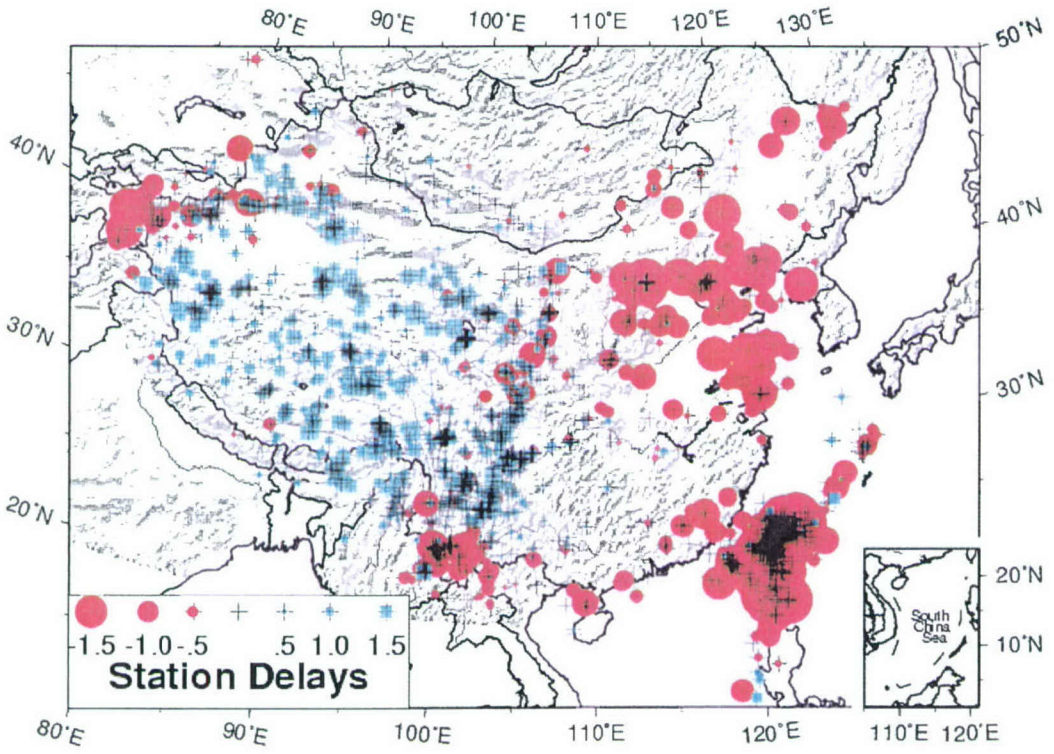

Figure 3-10. Final model of Pn event delays beneath China. Each second of relative travel-time delay corresponds to approximately 10 km of crustal thickness change.

SECTION 4

STATION SPECIFIC TRAVEL-TIMES

We have prepared travel-time curves for the CDSN stations in China (Figures 4-1). The two IMS stations in China, BJT and HIA, were not in existence when these data were collected; however, they replaced two nearby stations, BJI and HLR. We determined Pg, Pn, Sg, and Sn velocities for each of these stations via straight line fits (Table 4-1). The original phase identifications of the ABCE were used with no depth corrections. The ABCE identifies these phases to distances up to 9 degrees maximum.

Table 4-1. Intercepts and apparent velocities for Pg, Pn, Sg, and Sn phases at CDSN stations

Station	Location	Pg	Pn	Sg	Sn
BJI	Baijiatuan	-1.1s, 6.14km/s	4.99s, 7.91km/s	-0.56s, 3.66km/s	10.26s, 4.52km/s
ENS	Enshi	0.8, 6.17	8.6, 8.13	0.5, 3.54	11.1, 4.52
HLR	Hailar	-0.2, 6.06	6.9, 8.06	-0.4, 3.52	10.1, 4.51
KMI	Kunming	0.1, 6.17	7.0, 7.94	0.7, 3.58	10.9 4.45
LSA	Lhasa	0.3, 6.28	8.4, 8.02	0.4, 3.55	13.5, 4.52
LZH	Lanzhou	-1.1, 6.07	8.0, 8.00	-1.6, 3.53	12.7, 4.55
MDJ	Mudanjiang	-0.6, 6.09	6.28, 8.01	-1.9, 3.52	9.9, 4.5
QIZ	Qiongzhong	too little data			
SSE	Shanghai	-0.6, 6.09	poor data	-1.4, 3.53	9.1, 4.47
WMQ	Urumqi	0.7, 6.29	8.5, 8.08	0.7, 3.57	13.3, 4.55

numbers refer to intercept - velocity pairs in seconds and km/s

Pn velocities surrounding these stations vary from 7.9 to 8.1 km/s and Sn velocities are always 4.5 km/s. The lack of variation in Pn and Sn velocities is due to the large geographical averaging over a circle of 9 degrees radius (254 square-degrees). Pg velocities vary from 6.0 to 6.3km/s; Sg velocities vary between 3.5 to 3.7 km/s. Higher Pg velocities are at Lhasa and Urumqi, both regions of thicker crust.

Intercepts were also computed. Intercepts can be interpreted from the equation:

$t = (2z - d)\sqrt{\frac{1}{v_c^2} - \frac{1}{v_n^2}}$, where v_c is the crustal velocity above the refractor, v_n is the refractor velocity, z is the crustal thickness, and d is the average event depth. The square-root factor is approximately 1/10 s/km for Pn and 1/5.6 s/km for Sn. This was estimated using a 6.2 km/s crustal velocity and an 8.0 km/s mantle velocity and a conversion factor of 0.56 for the S-wave velocities. These numbers yield reasonable crustal thicknesses of 36 to 47 km if an average event depth of 10 km is assumed. For Pg and Sg, several stations have negative intercepts for Pg and Sg as a result of not compensating for event depth.

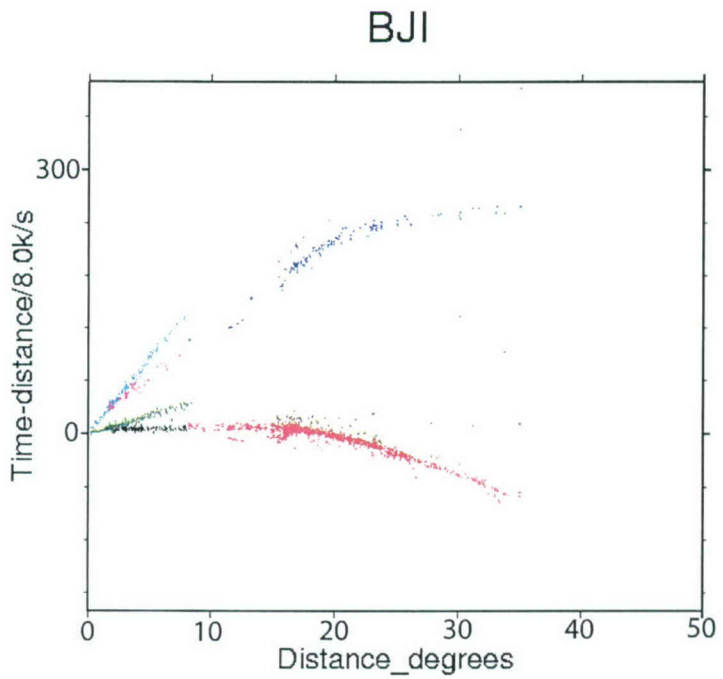
BJI
300
0
Time-distance/8.0k/s
0
10
20
30
40
50
Distance_degrees

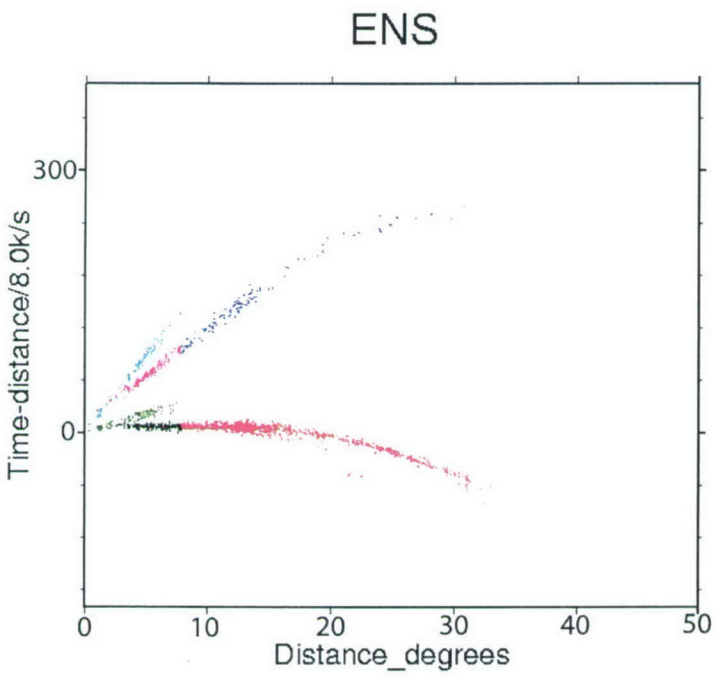
ENS
300
0
Time-distance/8.0k/s
0
10
20
30
40
50
Distance_degrees

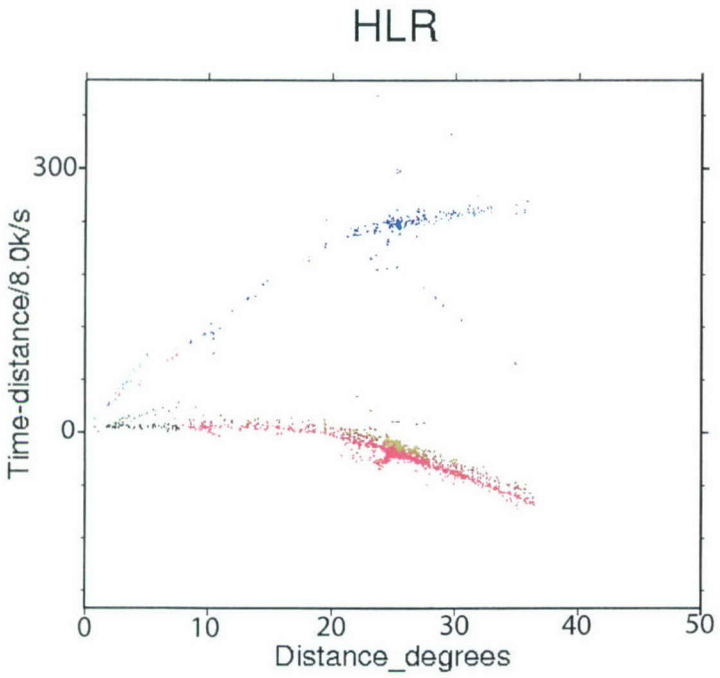
HLR
300
0
Time-distance/8.0k/s
0
10
20
30
40
50
Distance_degrees

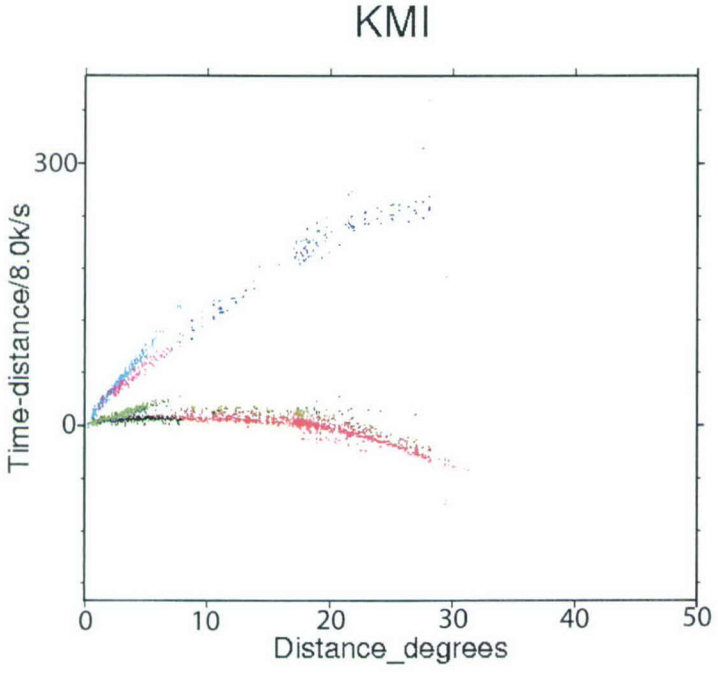
KMI
300
0
Time-distance/8.0k/s
0
10
20
30
40
50
Distance_degrees

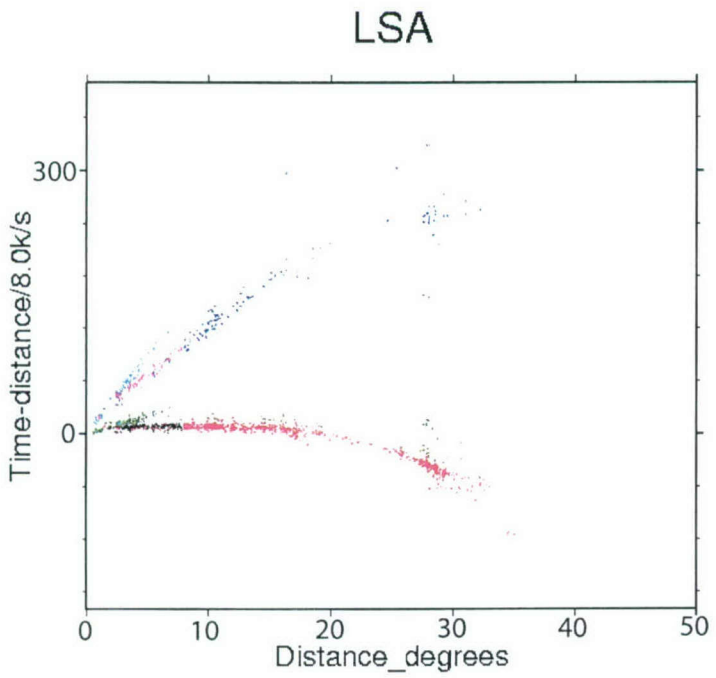
LSA
300
0
Time-distance/8.0k/s
0
10
20
30
40
50
Distance_degrees

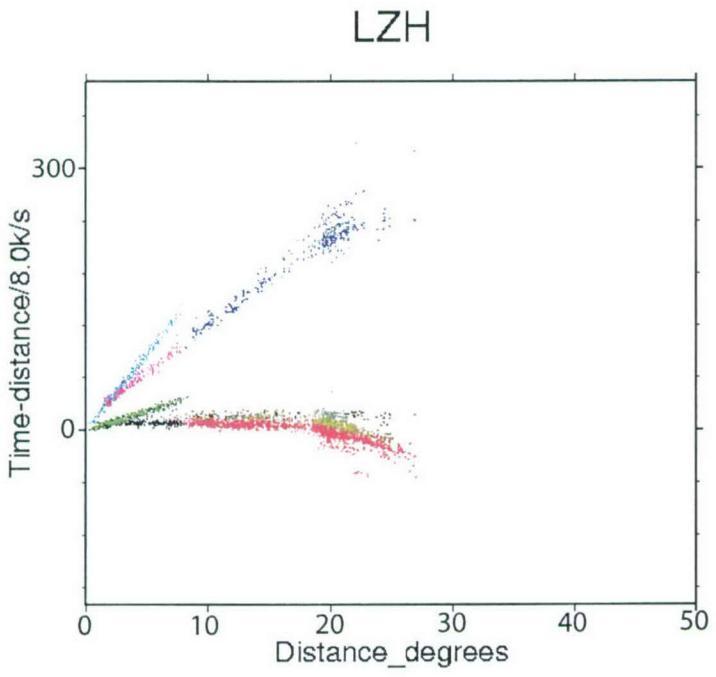
LZH
300
0
Time-distance/8.0k/s
0
10
20
30
40
50
Distance_degrees

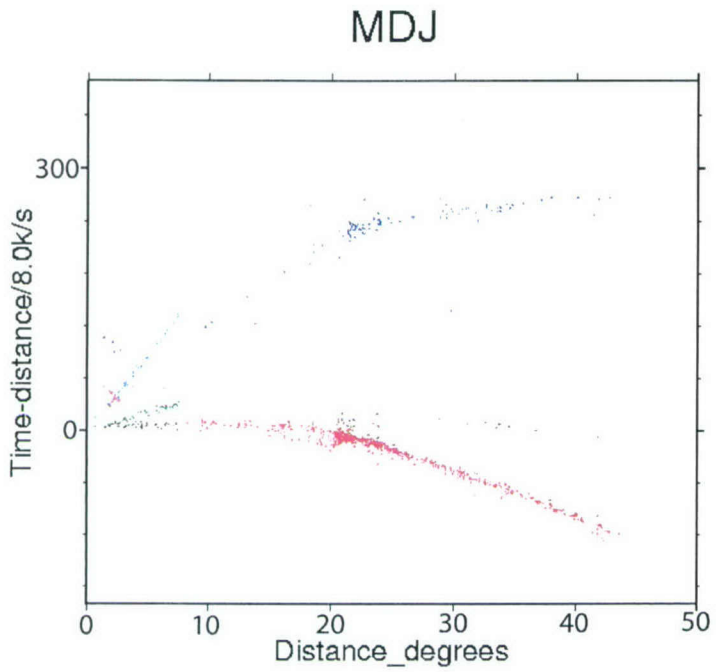
MDJ
300
0
Time-distance/8.0k/s
0
10
20
30
40
50
Distance_degrees

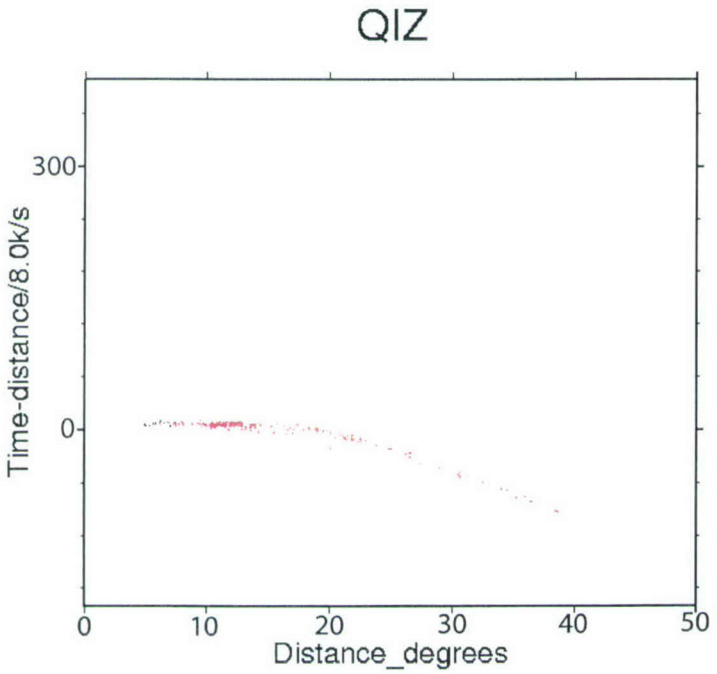
QIZ
300
0
Time-distance/8.0k/s
0
10
20
30
40
50
Distance_degrees

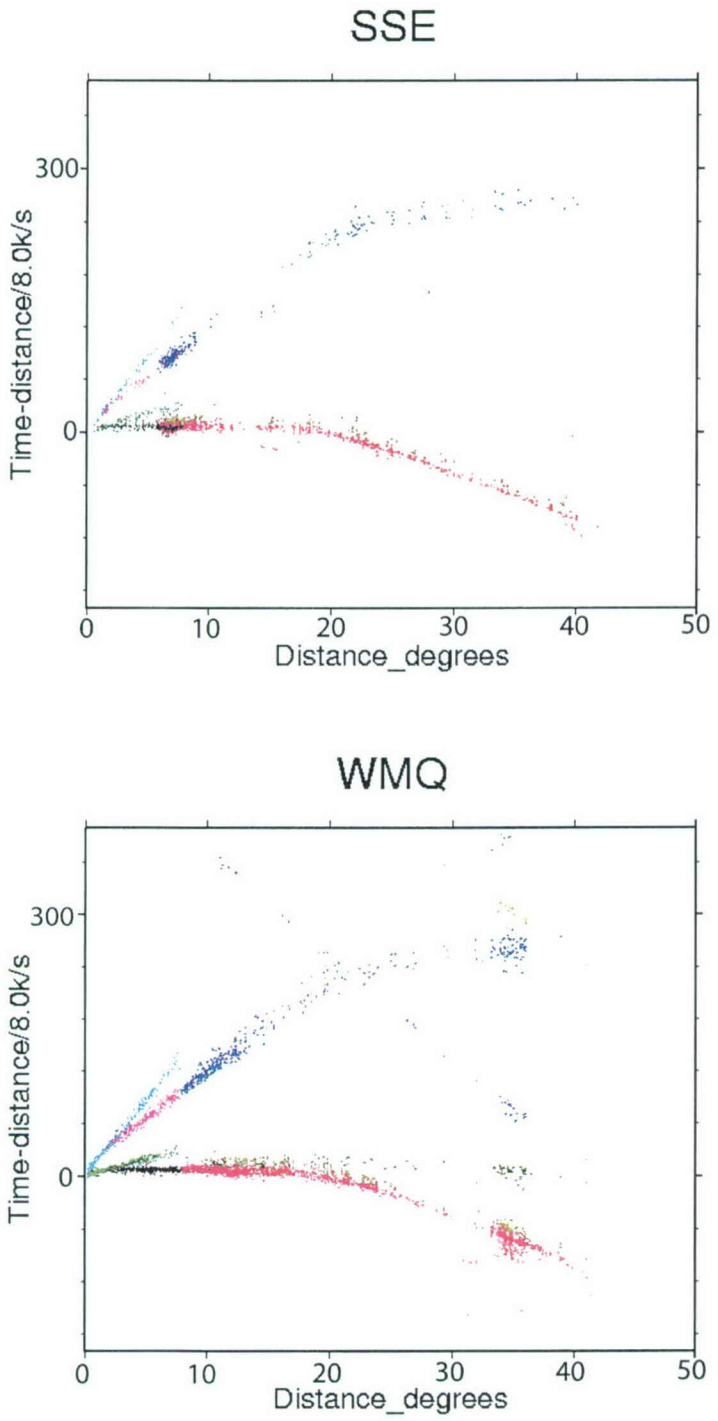

Figure 4-1. Reduced travel-time plots for ten CDSN stations. Stations BJI and HLR are next to IMS stations BJT and HIA. The ABCE routinely identifies arrivals as Pg, Pn, P, PP, pP, Sg, Sn, S, SS, sS, sP, PcP, S11, ScS, P11, ScP, and PcS.

SECTION 5

COMPARISON OF CHINESE EVENT LOCATIONS WITH PIDC LOCATIONS

We compared event locations from the ABCE with those reported by the Prototype International Data Center (PIDC). These two data sets overlap only for the year 1995. This is the first year of operation of the PIDC and the last year of data we have for China. We began by identifying ground truth events for the ABCE. We used the PDIC criteria for defining ground truth events: a GT25 event was recorded by at least 50 stations with a maximum azimuth gap of 90° and a GT10 event had at least 5 stations with a maximum azimuth gap of 180° within 3-degree distance (Yang and Romney, CMR Technical Report 99-15, 1999). These ground truth events were compared to locations from the PIDC Relocated Event Bulletin (REB). For the GT10 events, 23 of 91 events were reported by the PIDC (Figure 5-1). For the GT25 events, 86 of 89 events were reported by the PIDC (Figure 5-2). Events that were not reported by the PIDC were generally less than magnitude 4. On average, mislocations are less than 22 km distance, but several events are mislocated by over 33 km. The largest location difference was by 118 km for a magnitude 3.6 event on October 30, 1995 (8:26) in Yunnan province. For this event, the PIDC location used 5 stations with a 210° azimuth gap and lists standard errors of between 50 to 60 km. The PIDC depth was constrained to 0 km. The National Earthquake Information Center (NEIC) reported the event 101 km away from the ABCE location and the International Seismological Centre (ISC) reports the event 17 km away. Curiously, the location given to the ISC by Beijing was off by 14 km from the ABCE location that we obtained.

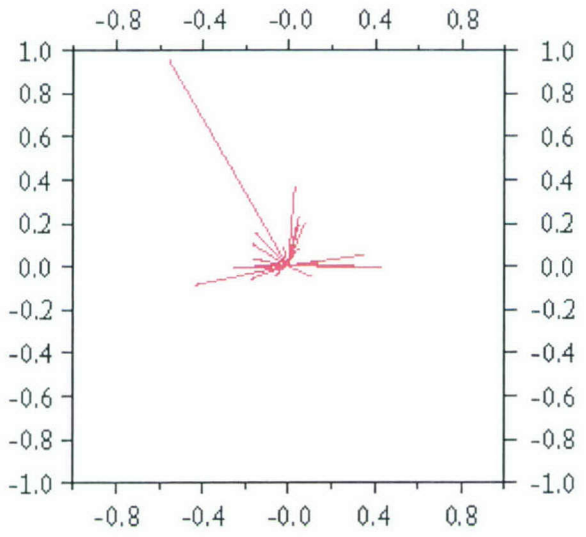

Figure 5-1. Relative locations from 23 GT10 events reported by both the PIDC and the Annual Bulletin of Chinese Earthquakes 1995. Axis scales are in degrees.

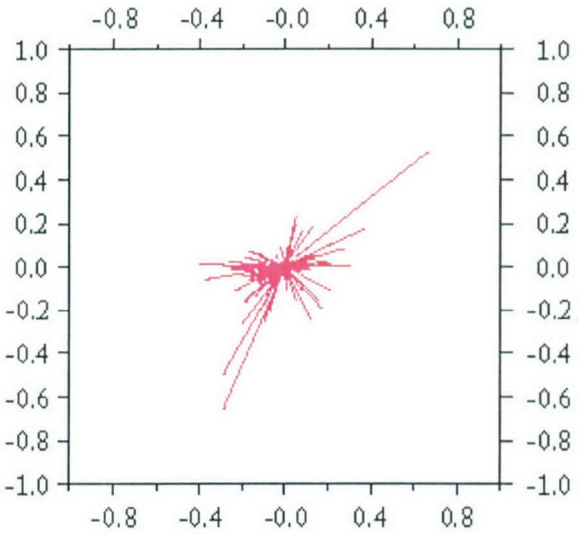

Figure 5-2. Relative locations from 86 GT25 events reported by both the PIDC and the Annual Bulletin of Chinese Earthquakes 1995. Axis scales are in degrees.

There were a limited number of ground truth events, so the entire 1995 ABCE catalog was searched for all events located by both the ABCE and PDIC. Histograms of earthquake size in China for 1995 are plotted for both the ABCE and the PIDC in Figure 5-3. These show that the ABCE locates slightly more events in all magnitude ranges than the PIDC. This discrepancy is from differences in the magnitude scales used by ABCE (local magnitude) and PIDC (body-wave magnitude). The plot deviates from linear for magnitudes less than 4.0 to 4.5 for both networks suggesting that smaller events are often missed by both catalogs.

We found 195 events that were located by both the ABCE and PIDC during 1995. Mislocation vectors for these are shown in Figures 5-4 and 5-5. Many of the events are in Taiwan, where the ABCE locations may not be as accurate. Differences between the ABCE epicentral locations and the equivalent PIDC locations average 0.95 degrees with a median of 0.55 degrees (Figure 5-6). The sample is biased by a few events with large location differences of up to four degrees. Events with extreme location differences of over three degrees were found to have limited station coverage, with five or fewer stations recording, and azimuthal gaps larger than 180 degrees. For the events in our sample, the estimated event location errors listed in the PIDC catalog averaged ±0.76 degrees. Considering the outliers in Figure 5-6, the PIDC error estimates are reliable. Poorly located events can be identified on the basis of their estimated error ellipses and the station coverage.

The CTBT requires that events be located within a 1000 km-squared region at the 2-sigma (95%) confidence level. The results find that this was not possible for the PIDC for most events during 1995 because of inadequate station coverage. This is also reflected in the large error estimates in the PIDC catalog. The best method to improve event location in China is to improve station coverage.

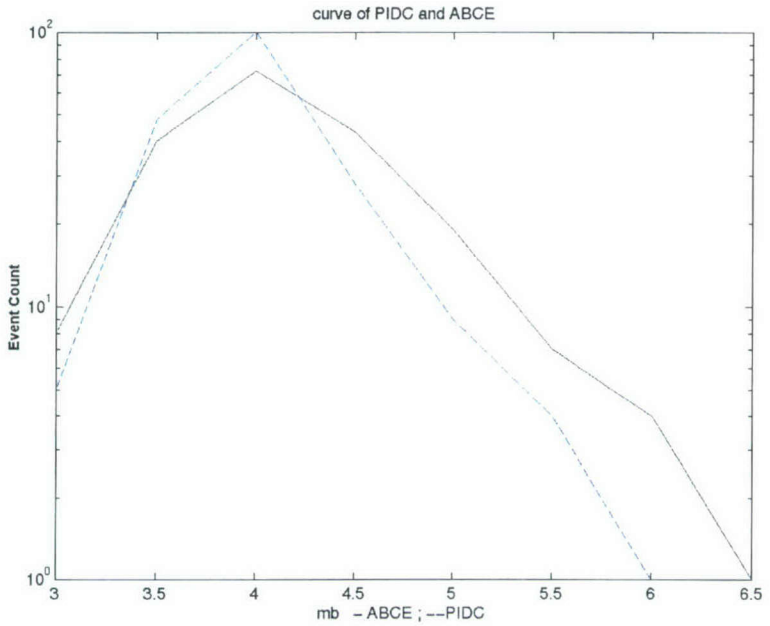

Figure 5-3. Histogram of event counts in different magnitude ranges for the Annual Bulletin of Chinese Earthquakes (ABCE) and the Preliminary International Data Center (PIDC) for 1995. The lower completeness threshold is between magnitude 4.0 and 4.5; some of the differences are due to differences in magnitude determination between the two catalogs.

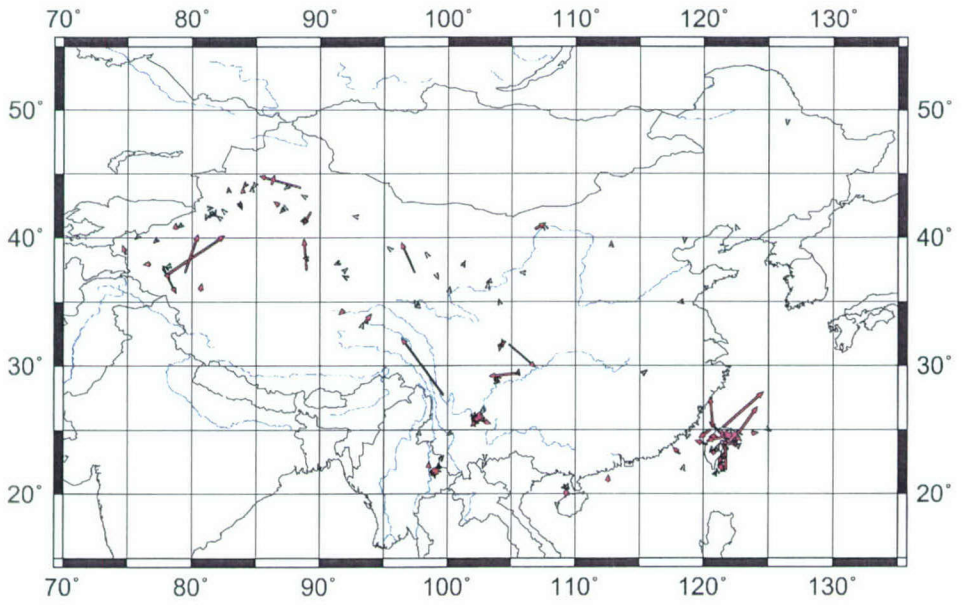

Figure 5-4. Map showing location differences between the ABCE and PIDC catalogs for China for 1995. Arrows begin at the ABCE location and end at the PIDC location.

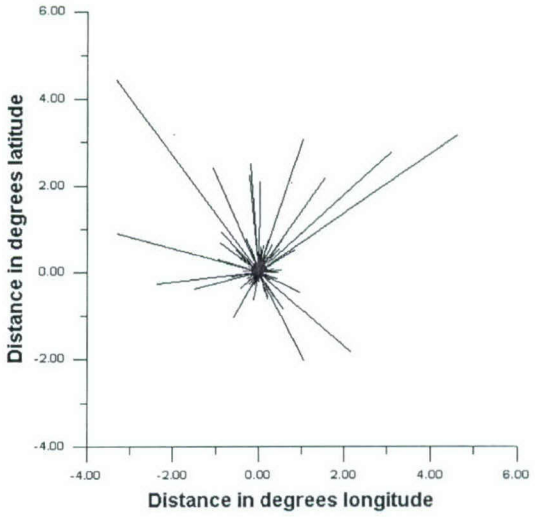

Figure 5-5. Composite plot of 195 location difference vectors between ABCE and PIDC for China 1995. Vectors point from the ABCE location to the PIDC location. Axis scales in degrees distance.

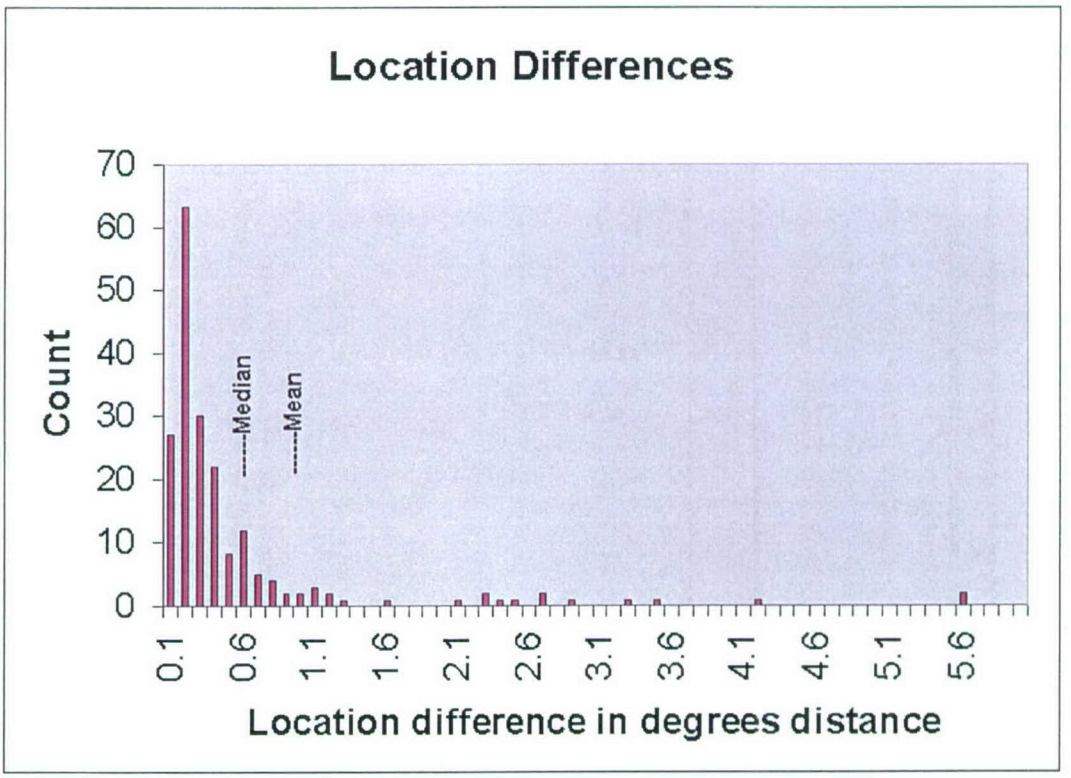

Figure 5-6. Histogram of location differences between the ABCE and PIDC locations for China, 1995. The average location difference is 0.95 degrees; however, this is biased by a few poorly located events. The median location difference is 0.55 degrees and the most probable location difference is 0.1 degrees.

SECTION 6

PROPAGATION CHARACTERISTICS OF SN AND LG IN NORTHEASTERN CHINA AND MONGOLIA

We present propagation characteristics of the short-period seismic phases Sn and Lg in Northeastern China and Mongolia. Richard Rapine and James Ni have submitted this section of the report to the Bulletin of the Seismological Society of America. Three-component broadband and short-period seismograms from the Global Seismic Network station ULN and the Chinese Digital Seismic Network stations BJT, HIA, and MDJ were used in this study. The digital waveforms were bandpass filtered (1.0-5.0 Hz) and were used to rank Sn and Lg amplitudes relative to the Pn and Pg phases. The short-period Sn waveforms exhibit great variability. Efficient Sn propagation is observed in Southern Siberia and along the Daxinganling Mountains. Inefficient Sn transmission is found near Lake Baikal and most of Northeastern China. Sn does not propagate across Mongolia or the North China Plain. In Northeast China, zones of attenuation exist within regions of extension and high heat flow. In Mongolia, severe Sn attenuation suggests the presence of a partially melted uppermost mantle. The zones of inefficient Sn propagation coincide with zones of low Pn velocities (7.9 km/s) determined by Wu (1998). In contrast, the Lg seismic phase has large amplitudes and propagates efficiently for all distances in Northeastern China and Mongolia.

Heterogeneity and anelasticity of the crust and upper mantle cause amplitude reduction of regional seismic phases. Measurements of this loss in amplitude can be used to infer the physical properties and structure of a particular region on earth. The propagation of short-period regional Sn and Lg waves in Northeastern China, Mongolia, and Southern Siberia is characterized here and used to investigate how tectonic and geologic structures affect these regional phases. This study utilizes the digital broadband and short-period data from the Global Seismic Network (GSN) station ULN (Ulaanbaatar, Mongolia) and the Chinese Digital Seismic Network (CDSN) stations BJT (Beijing, China), HIA (Hailar, China), and MDJ (Mudanjiang, China). Propagation efficiencies of Sn and Lg phases were qualitatively analyzed by ranking their amplitudes relative to the Pn and Pg phases. The data were then used to determine the areas of Sn and Lg attenuation in the region of Northeastern China and Mongolia.

The North China Plain and the Songliao Basin of Northeastern China are large Cenozoic extensional structures (Ren et al., 1987). The locations of these basins coincide with areas in which the lithosphere is thinned and high heat flow is present. These basins represent the effects of Mesozoic-Cenozoic (Songliao Basin) and Cenozoic crustal extension (Western North China Plain) proceeded by Andean-type subduction, related deformation and magmatism. The magmatic arc during the Mesozoic subduction episode modified the Daxinganling Mountains. It has been suggested that the cause of extension was the upward advection of the asthenosphere, which was related to the foundering of the Kula-Pacific plates beneath the Eastern Asia continental margin since the late Mesozoic time (Ren et al., 1987).

Variations in the structure and properties of the crust and uppermost mantle greatly affect short-period seismic waves recorded at regional distances (200-2000 km). Lg waves, which are

composed of shear waves that have been trapped in the crust, have characteristics that are diagnostic of the crustal structure. In contrast, Sn waves travel in the mantle lid and are indicative of the physical properties there. Changing of signal-to-noise amplitude ratios of these regional phases can provide insight into where these variations occur. Since regional seismic phases are used for discriminating nuclear explosions from earthquakes (e.g., Taylor et al., 1989), it is important to know where these phases are attenuated. Major structural features such as sedimentary basins, rapidly changing surface and Moho topography will all influence the character of regional seismograms (e.g., Gibson and Campillo, 1994). It is clearly important to map where these features affect the propagation of regional seismic phases. This kind of regional data is an integral part of the effort toward verification of a Comprehensive Test Ban Treaty (CTBT).

Figure 6-1 shows the seismic station and event locations used in this study. These stations are part of the Chinese Digital Seismic Network (CDSN) and Global Seismic Network (GSN). Table 6-1 summarizes the station information and includes the years of data we analyzed from each station. Short-period data were obtained from stations BJT, HIA, and MDJ in China. Broadband data were obtained from ULN in Mongolia. The broadband data were recorded on a three-component Streckeisen STS-1 instrument. The STS-1 records data at 20 samples/s and has a flat amplitude response from .01 to 10 Hz. Short-period data were recorded by Model DJ-1 seismometers at 40 samples/s. The seismic events requested from the Incorporated Research Institutions for Seismology Data Management Center (IRIS DMC) had body-wave magnitudes greater than 4.3, epicentral distances between 2 and 15 degrees, the complete range of backazimuths, and depths less than 50 km. Event origin times and locations were taken from the Preliminary Determination of Epicenters (PDE) catalogs distributed by the U.S. Geological Survey (USGS). All data with low signal-to-noise ratios were removed from the data set used for this analysis.

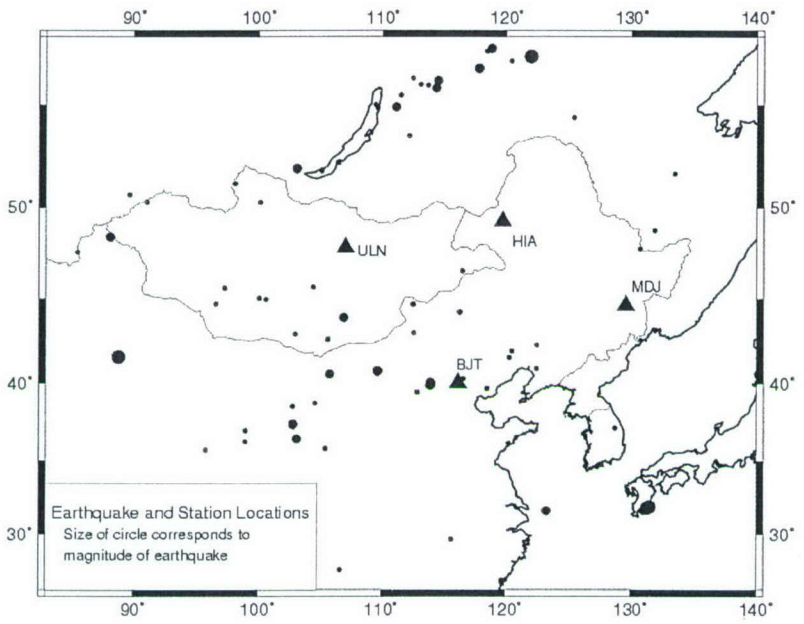

Figure 6-1. A station and event location map for the region of study. Triangles represent CDSN and GSN station locations. Circles represent event locations and are proportional to the event magnitudes.

Short-period and broadband data were used to study the regional wave propagation of Sn and Lg phases in Northeast China and Mongolia. The high-frequency propagation efficiencies of these phases were used to learn more about the structure and composition of the crust and upper mantle in the area of interest. This approach has been used many times before for different geologic regions (e.g., Kadinsky-Cade et al., 1981; Rapine et al., 1997; Rodgers et al., 1997). A bandpass filter was used to filter the data between 1.0-5.0 Hz.

Table 6-1. Summary of the stations, recording period of data and type of data.

Station Name	Lat(°N)	Lon(°E)	Data Period	Type*
BJT	40.10	116.17	1994-1997	SP
HIA	49.27	119.74	1988-1996	SP
MDJ	44.62	129.59	1989-1996	SP
ULN	47.87	107.05	1994-1997	B

* SP = short-period, B = broadband

Sn waves predominantly travel within the uppermost mantle and since they are shear waves, they are more sensitive to attenuation than P waves. At regional distances, Sn arrives with a group velocity of 4.4-4.7 km/s. Sn propagation efficiencies have been used to infer the physical properties of the mantle lid. For example, Sn generally does not propagate across regions of high heat flow such as the Basin and Range Province and the central/northern Tibetan Plateau (e.g.,

Ni and Barazangi, 1983; Beghoul et al., 1993; McNamara et al., 1995). Poor Sn propagation may be attributed to high shear wave attenuation associated with a partially melted mantle lid (Molnar and Oliver, 1969). Efficient Sn propagation is observed beneath stable shield regions (e.g., Brune and Dorman, 1963; Bath, 1966).

Lg waves are a complex, high-frequency wavetrain with large amplitudes at regional distances and group velocities from 3.2 to 3.7 km/s. Lg has been modeled as a composite of higher-mode Love and Rayleigh waves. In terms of ray theory, Lg can be considered as a sequence of multiply reflected, postcritical S waves trapped in the continental crust (Bouchon, 1982). Lg propagates efficiently in continental shields but is not seen across ocean basins due to the thin oceanic crust (Press and Ewing, 1952). The amplitude of Lg may be weakened by variations in crustal structure along the propagation path or by a low-Q or partially melted crust (Ruzaikin et al., 1977; Campillo, 1987; Husebye and Ruud, 1996).

The high signal-to-noise data were used to manually pick the regional phase arrivals of Sn and Lg. We picked the arrival times of Sn and Lg to coincide with group velocities of 4.5 km/s and 3.5 km/s, respectively. Previous studies analyzed short-period seismograms to qualitatively characterize broad tectonic regions in terms of efficient or inefficient Pn, Sn, and Lg propagation (e.g., Ruzaikin et al., 1977; Kadinsky-Cade et al., 1981; Ni and Barazangi, 1983; Rodgers et al., 1997). We used a similar approach to rank the efficiencies of the observed regional phases. We classified efficient Sn and Lg phases as those phases with signal-to-noise (S/N) ratios greater than or equal to two. Sn and Lg phases with S/N ratios between one and two were classified as inefficient. When no Sn or Lg phase can be seen on a seismogram, we classified that phase as not propagating for that station-event path.

6.1 RESULTS.

Representative short-period seismograms recorded by CDSN stations are provided in Figures 6-2 and 6-3. Efficient Sn propagation is observed in Southern Siberia and the Daxinganling (Figure 6-4). Apparently, the lithosphere beneath this mountain is sufficiently cooled and does not contain partial melt. Poor Sn transmission is found in Lake Baikal and most of Northeastern China where late Mesozoic to Cenozoic extension has occurred (Figure 6-5). Sn does not propagate across Mongolia and most of the North China Plain, where Late Tertiary to Quaternary volcanism exists (Figure 6-6). Rapine et al. (1997) also observed no Sn propagation across Mongolia from earthquakes that occurred in Siberia and recorded at stations in China. The strong Sn attenuation beneath the North China Plain and Mongolia suggests that there is partial melt in the uppermost mantle beneath those regions.

High-frequency Lg waves propagate efficiently in Southern Siberia, Northeastern China, and Mongolia (Figure 6-7). In this region of study, there were no observations of Lg blockage or attenuation. Lg amplitudes remained large for even the longest distances studied. Figures 6-2 and 6-3 show the large Lg amplitudes relative to other phases and the noise. Structural boundaries in the crust in this region do not have a large effect on Lg propagation as they do in such regions as the Tibetan Plateau.

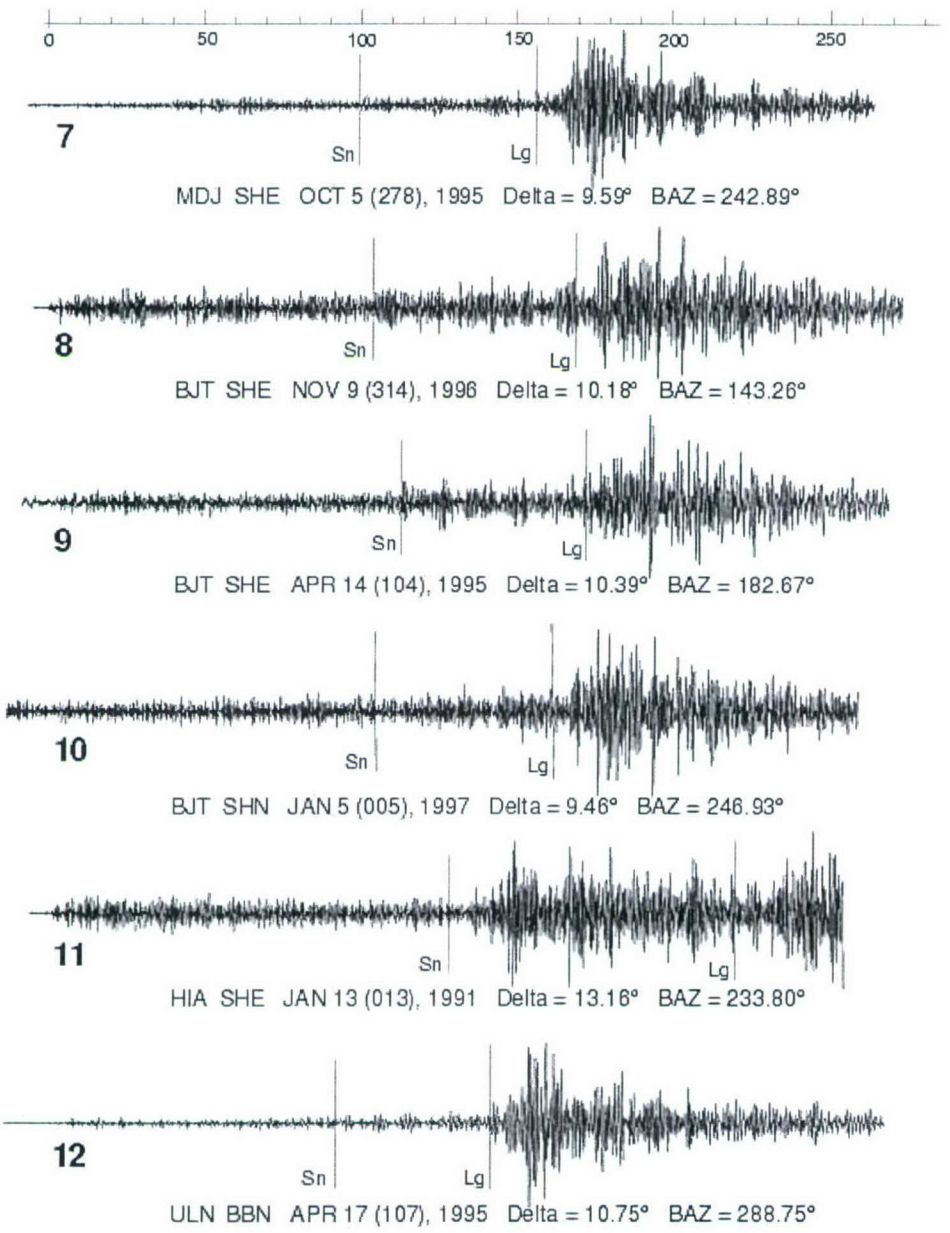

Figure 6-2. Representative seismograms from a short-period CDSN station. A time axis is provided at the top of the figure, zero corresponds to the Pn arrival time. Vertical bars represent the expected arrival time of Sn or Lg. All seismograms were bandpass filtered between 1.0-5.0 Hz.

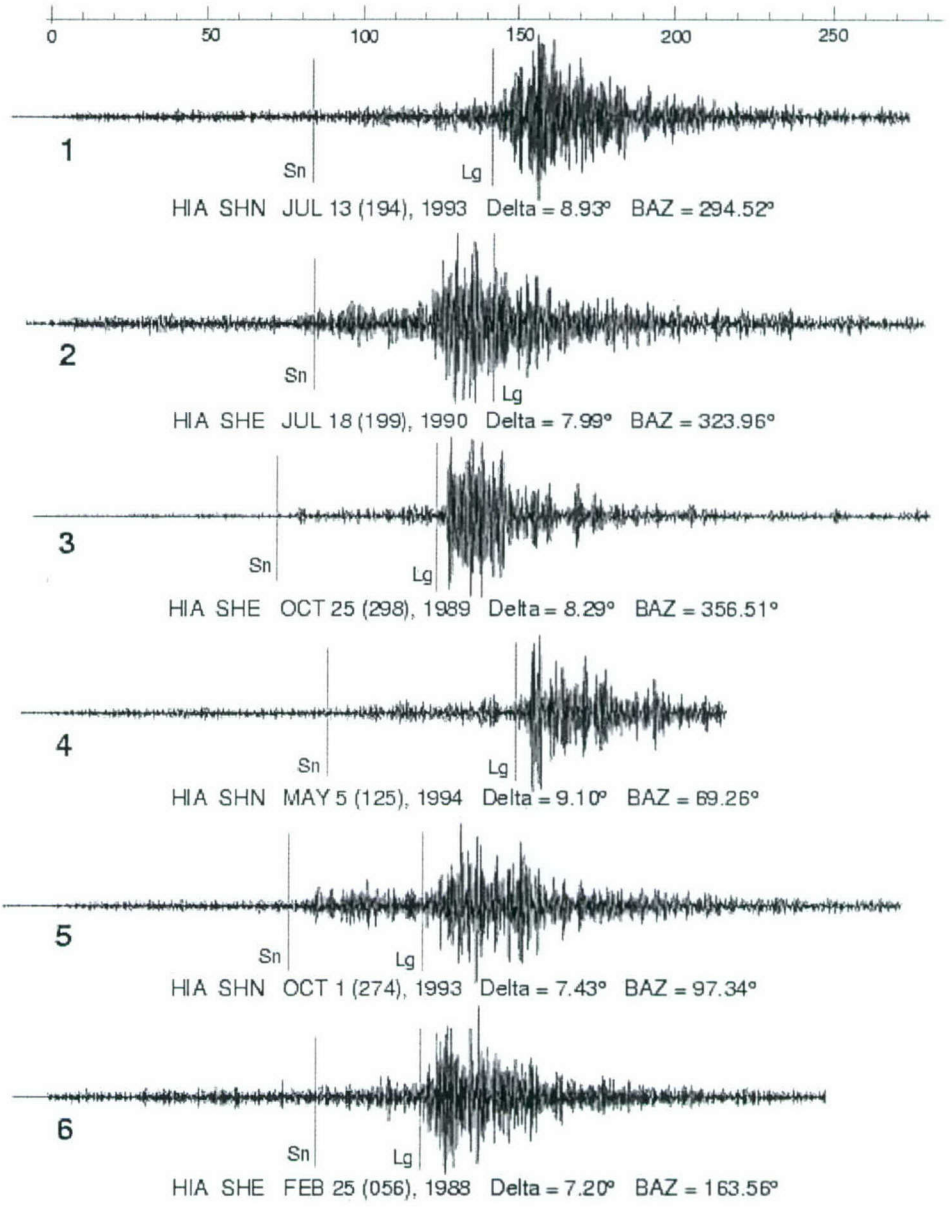

Figure 6-3. Representative seismograms from short-period and broadband stations of the CDSN and GSN, same as Figure 2.

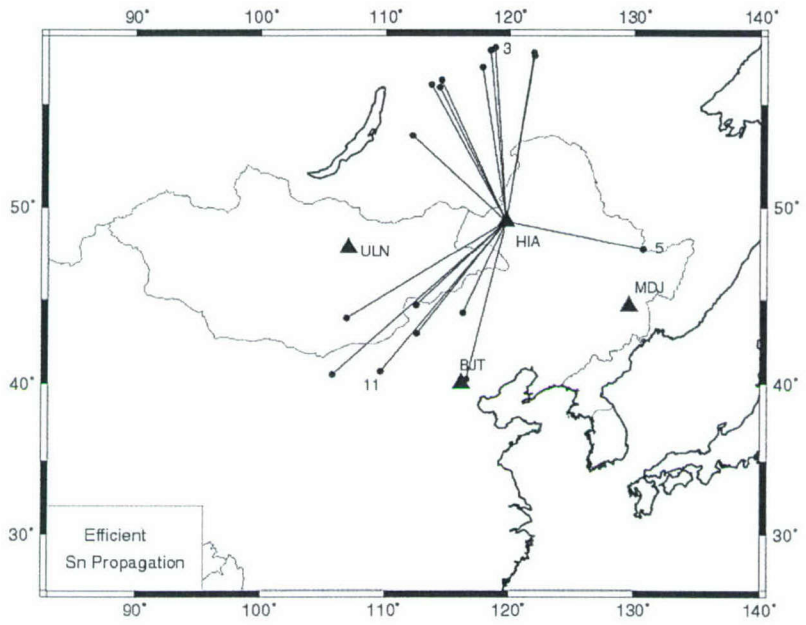

Figure 6-4. A map of efficient Sn wave propagation in China, Mongolia and Southern Siberia. Triangles represent station locations, circles represent event locations and the numbers refer to seismograms from Figures 2 and 3.

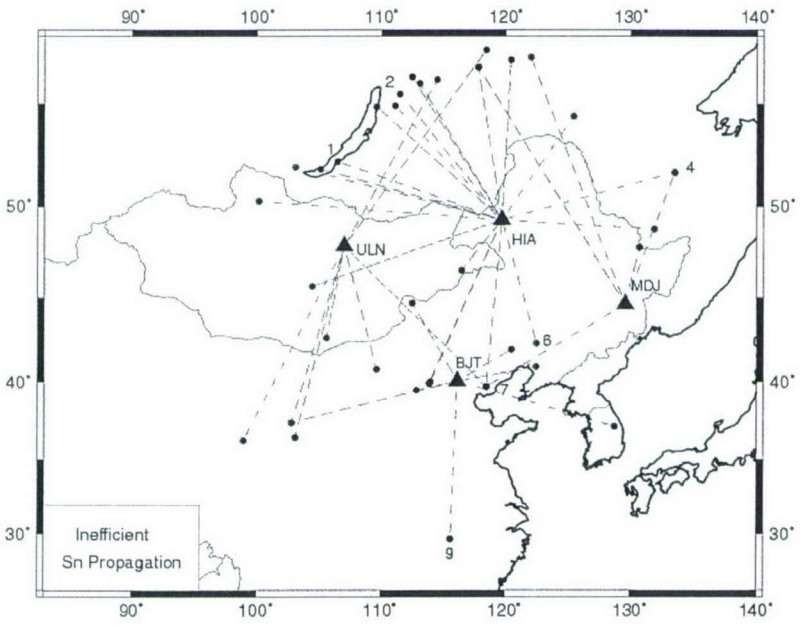

Figure 6-5. A map of inefficient Sn wave propagation paths. Triangles represent station locations, circles represent event locations and the numbers refer to seismograms from Figures 2 and 3.

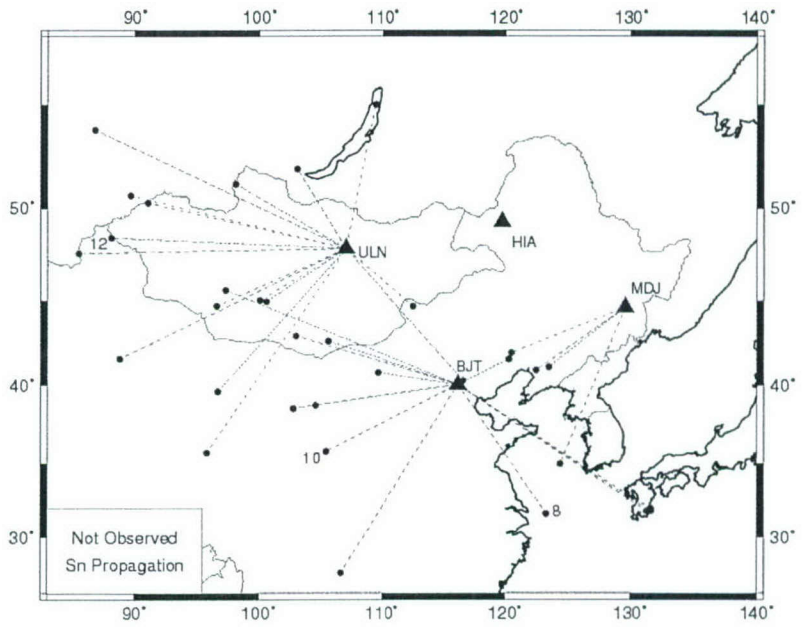

Figure 6-6. A map shows the station-event paths where no Sn propagates. Triangles represent station locations, circles represent event locations and the numbers refer to seismograms from Figures 2 and 3.

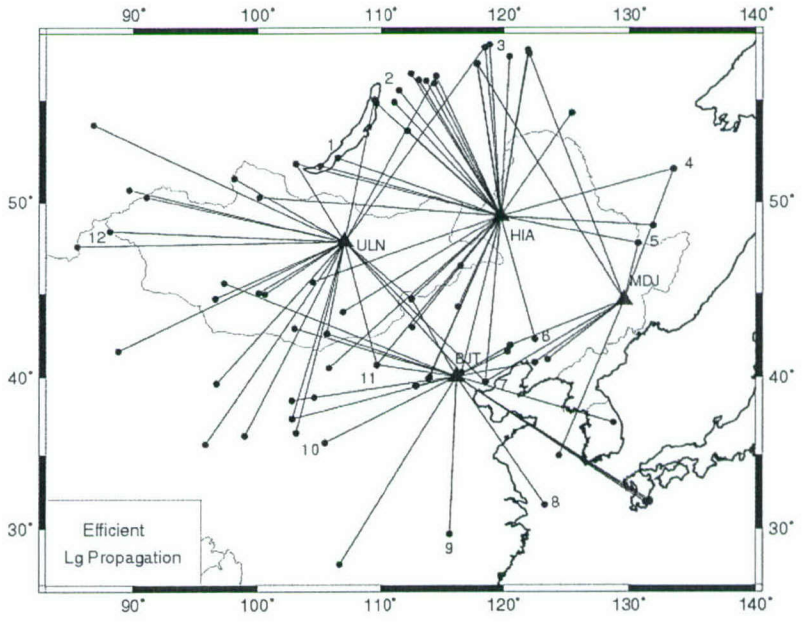

Figure 6-7. A map of efficient Lg wave propagation in China, Mongolia and Southern Siberia. Triangles represent station locations, circles represent event locations and the numbers refer to seismograms from Figures 2 and 3.

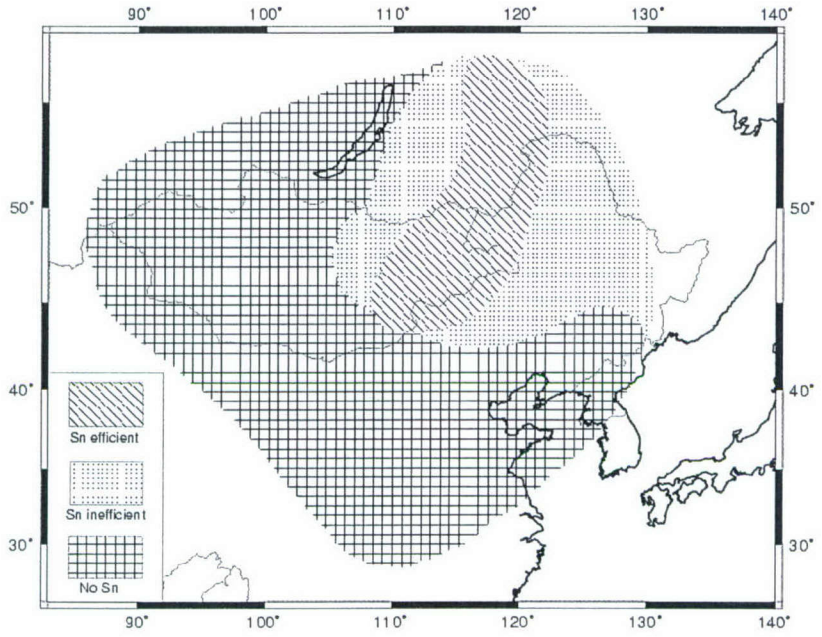

Figure 6-8. A summary map of efficient, inefficient and no Sn wave propagation in Northeast China and surrounding regions.

6.2 DISCUSSION.

The propagation efficiencies of Sn and Lg waves have been mapped for Northeast China and Mongolia. A summary map of the gross characteristics of short-period Sn regional waves has been provided in Figure 6-8. This map provides some insight into the uppermost mantle properties of the region and explicitly shows the regions of attenuation we observed. Lg propagates efficiently and shows large amplitudes for all paths studied in the region. The Cenozoic tectonics of Northeast China has had an influence on short-period Sn wave propagation. A P wave study of the upper mantle beneath Northern China and Mongolia measured low P wave velocities in the uppermost mantle (7.9 km/s) in most of the region of our study (Wu et al., 1998). This Sn study provides evidence that the uppermost mantle may be partially melted in parts of Mongolia and Northeast China. A buoyant mantle beneath the Mongolian Plateau would support the high topography observed there. Any partially melted mantle is probably a result of either convective removal of part of the mantle lid or prior subduction (Paleozoic) of water-rich materials into the upper mantle leading to a present weakening and melting due to strain heating. This strain heating is probably a result of the Indian-Eurasian collision whose effects have been felt all the way up to Siberia (e.g., Tapponnier and Molnar, 1977).

SECTION 7

LATERAL VARIATION OF LG ATTENUATION IN TIBETAN PLATEAU

7.1 INTRODUCTION.

Lg is a crustal guided wave propagating efficiently for several thousands of kilometers in stable continental shields with the group velocities between 3.7 and 3.0 km/s. Modeling of *Lg* has shown that it is the sum of higher mode surface waves or superposition of multiply reflected shear waves within the crust (Bouchon, 1982; Kennett, 1986). The characteristic of *Lg* phase is sensitive to changes within the crustal wave-guide such as sedimentary basins and large lateral variations in depth to Moho and in crustal seismic velocity structure (Ruzaikin et al., 1977; Campillo, 1987). Press and Ewing (1952) found that Lg does not propagate within thin oceanic crust, while the presence of *Lg* phase is often associated with path traveling within continent (Oliver et al., 1955). *Lg* attenuation is caused by two main sources: scattering due to heterogeneities and intrinsic absorption. Many attempts have been made to separate these contributions (e.g. Mayeda et. al., 1992). Their results indicate that the proportion of each contribution might be different for different regions.

Tibet is the one of the most striking example of continent-continent collision. The collision began about 50 Ma causing the Tibetan Plateau rising to its 5 km elevation. Although *Lg* is one of the most dominant phases observed on regional seismograms for paths traveling within continental shield, studies in Tibet shows that the maximum distance to observe *Lg* wave is about 600 km within the Plateau (McNamara, 1996). Beyond that distance, *Lg* energy is largely attenuated. There have been a number of studies to find *Lg* attenuation in Tibet. Ni and Barazangi (1983) qualitatively mapped the *Lg* attenuation where they found inefficient *Lg* in the plateau. Rapine et al. (1996) found that *Lg* is generated in Tibet, however, paths to LSA (Figure 7-1) exhibits large attenuation. They also suggested that the plateau boundaries causes scattering of *Lg* energy. Although, high attenuation in Tibet is well known, none of the methods could find *Lg* Q_0 values much less than 200 for Tibetan Plateau (Reese et al., 1999). Xie (2002) used two-station method allowing backazimuthal gap up to 36^0 and found *Lg* Q_0 =126 for Eastern Tibet. He averaged all two-station measurements to obtain an average *Lg Q*. Because high frequency Lg is rapidly attenuated in areas of very low Q, it is especially difficult to quantify areas of low Q such as those in Southernmost Tibet because the lack to stations in Tibet. In this study, we use data from several experiments conducted within Tibet and applied two different techniques to determine the lateral variation of *Lg Q* within Tibet (Gok et al., 2004). We also mapped the presence of lateral change along the profiles of INDEPTH II and INDEPTH III.

7.2 DATA AND METHOD.

During the period of 1991-1999 there were three PASSCAL temporary broad-band seismic experiments to explore the crustal and upper mantle structure of Tibet (Figure 7-1). The first one was the 1991-1992 IRIS-PASSCAL experiment, a one-year deployment in the eastern part of Tibet with 11 broad-band stations. The second one was INDEPTH II extending from the High Himalayas to about 150 km north of the IYS (Indus-Yarlung Suture). Nine of the fifteen stations equipped with broad-band CMG-3T seismometers. The remaining six stations were equipped

with 1 Hz short period seismometers. The third experiment, INDEPTH III, operated for one year (July, 1998-June, 1999) across the Bangong-Nujiang Suture (BNS) with more stations (37 broadband, 10 semi-broadband and 15 short-period stations). INDEPTH II and INDEPTH III provided a unique opportunity to measure the lateral variation of *Lg* attenuation in Tibet.

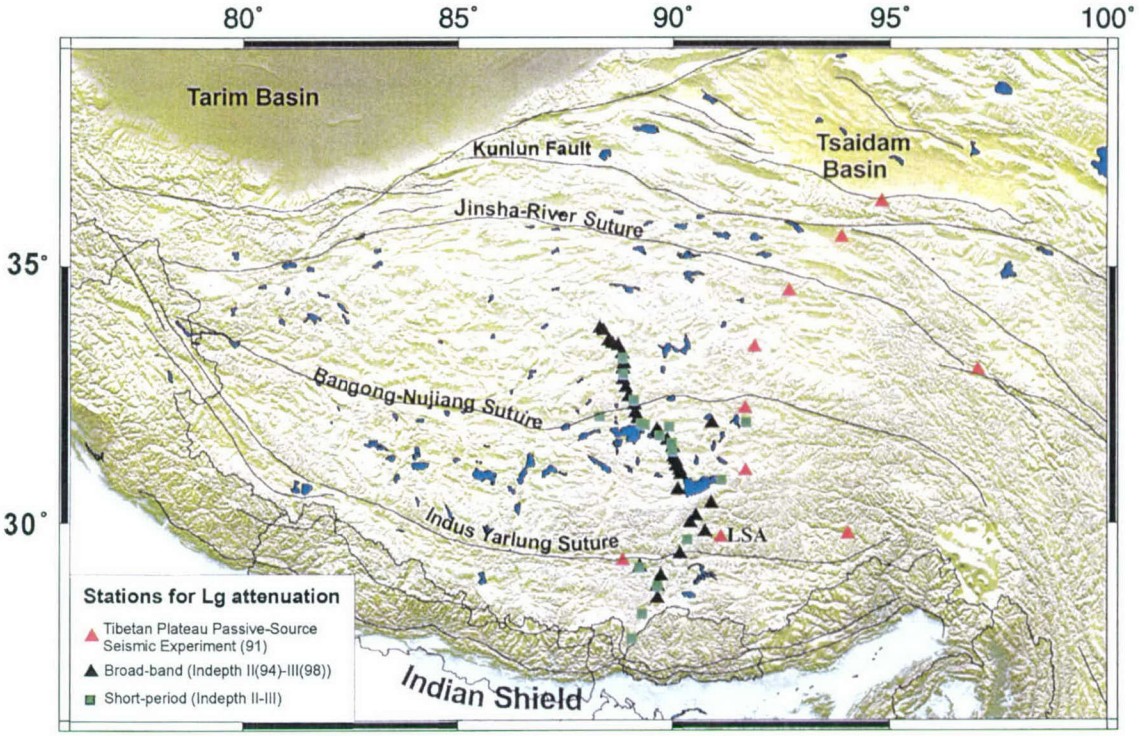

Figure 7-1. Station distribution of seismic experiments during period of 1991-1999.

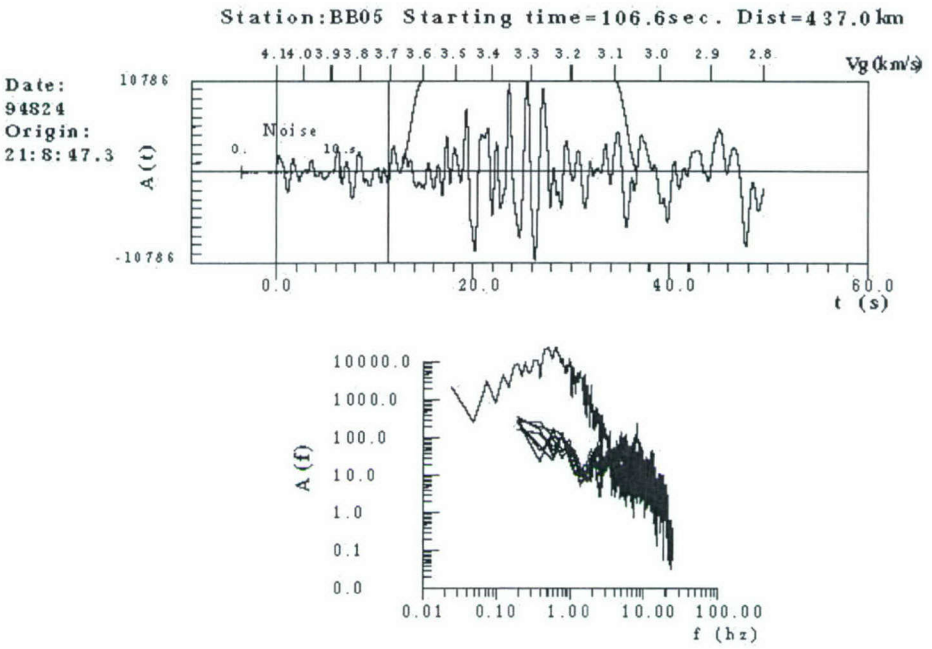

Figure 7-2. Lg wave package and noise part spectra of event 1994 236.

We analyzed ten earthquakes from INDEPTH II, eleven from 1991-1992 PASSCAL experiment and six from INDEPTH III. All selected earthquakes have crustal depths. We used only vertical component seismograms within distances of 2^{o} to 6^{o}. The earthquake magnitudes range between $4.0 \leq Mb \leq 5.5$. The *Lg* group velocity window is set between 3.7-3.0 km/s depending on the wave package (Figure 7-2). In this study, we used two different frequency domain techniques to estimate *Lg* attenuation in Tibet. Both methods have been extensively tested on earthquakes and explosions (Xie 1993, 1998).

7.3 STOCHASTIC-SPECTRAL INVERSION OF LG Q_0.

Nuttli (1973) first used *Lg* amplitudes in the time domain to measure path attenuation and the size of the seismic source. In frequency domain, the spectral inversion method of Xie (1993) was developed to simultaneously invert for source and path variable Q unlike the other inversion methods which were based on either an assumption of constant Q or separately measured source and attenuation terms. *Lg* displacement amplitude spectra can be expressed as a product of terms in frequency domain at i^{th} station,

$$A_i(f) = S(f)G(\Delta)R_i(f)X_i(f)\exp\left(-\frac{\pi f^{1-\eta_i}\Delta_i}{V_{Lg}Q_i(f)}\right) \tag{7.1}$$

using the frequency dependency of Lg,

$$Q(f) = Q_0 f^{\eta} \tag{7.2}$$

where S(f) is the source spectrum assuming *Lg* is not effected by the radiation pattern and can be written as,

$$S(f) = \frac{M_0}{4\pi\rho v_s^3} \frac{1}{1 + f^2 / f_c^2} \tag{7.3}$$

where ρ and v are the averaged crustal density and shear-wave velocity, respectively (Street et al., 1975). G()) is the geometrical spreading term, $\sqrt{\Delta_0 \Delta_i}$, where Δ_0=100 km. X(f) is site response and R(f) is randomness due to propagation such as random effects of multiple ray *Lg* arrivals and/or 3D heterogeneity. Using the above relation we end up with the model vector

$$m^T = (M_0, f_c, Q_{01}, \eta_1, ..., M_N, f_N, Q_{0N}, \eta_N)^T \tag{7.4}$$

The radiation pattern, systematic deviation in velocity structure, station site response and systematic deviation from w^{-2} model is ignored. Equation (7.1) is linearized by taking the logarithm of both sides. For a single event recorded by N stations, unknowns are estimated by grid searching over the possible M_0 and f_c using the following relationship,

$$\ln\left[-\frac{V_{Lg}}{\pi \tau_i \Delta_i} \ln\left(\frac{A_i(f) G(\Delta)}{S(f)} \right) \right] = (1 - \eta_i) \ln f - \ln(Q_{oi}) + e_i(f), \qquad i = 1, 2, ..., N \tag{7.5}$$

Q_{0i} and 0_i are estimated over this loop, and the complete model vector is used to estimate a residual square,

$$\mathrm{Re}\, s^2 = \sum_{i=1}^{i=N} \sum_{j=1}^{j=J(i)} \left(\ln[\sqrt{\Delta_0 \Delta} A_i(f_j)] - \ln\left[S(f_j) \exp\left(-\frac{\pi f_j^{1-\eta_i} \Delta_i}{V_{Lg} Q_{0i}} \right) \right] \right)^2 \tag{7.6}$$

The residual square is estimated for the all possible M_0 and f_c values. The model vector that minimizes the solution is the best solution (Xie, 1998).

7.4 TWO-STATION INVERSE METHOD.

The two-station spectral ratio method is a very robust technique of measuring attenuation since it properly eliminates source effects and results in a less biased estimate of *Lg* Q_0. In this method, the pair of stations is selected so that they lie on the same great circle path as from the source. The *Lg Q(f)* in the study area is assumed as being laterally homogeneous. When an event is recorded by two stations, j1 and j2, along the same great circle path, we denote the *Lg* amplitude spectra recorded at the station j as A_j (j = j1,j2), and define a scaled logarithmic spectral ratio

$$D(f) = \frac{V_{Lg}}{\pi (R^{j2} - R^{j1})} \ln\left[\frac{\sqrt{R^{j1}} A(f)^{j1}}{\sqrt{R^{j2}} A(f)^{j2}} \right] \tag{7.7}$$

where Vg is the *Lg* group velocity, R(j1) and R(j2) are the epicentral distances. For each of the station pairs (j1, j2), the number of events that are recorded along the same great circles as I (j1, j2). The mathematical expectation was given by (Xie and Mitchell 1990; Xie, 2002)

$$E(D_l) = \frac{f_l}{Q_{Lg}(f_l)} \tag{7.8}$$

$$\ln(D_l) = -\ln Q_0 + (1-\eta)\ln(f_l) \tag{7.9}$$

7.5 LATERAL VARIATION OF LG ATTENUATION .

The Algebraic Reconstruction Technique (ART) is a way of imaging lateral changes of velocities or amplitudes. Xie and Mitchell (1990) applied an imaging algorithm that is originally for the regionalization of *Lg* coda Q estimates. We adopted this technique for use here. Since we aim to resolve only the change along the array we used only the 1D imaging.

The ART technique can be briefly summarized as follows,

$$\Delta_n^i = \frac{S_n}{Q_n} - \sum_{m=1}^{N_g} \frac{1}{Q_m^i} s_{mn} \tag{7.10}$$

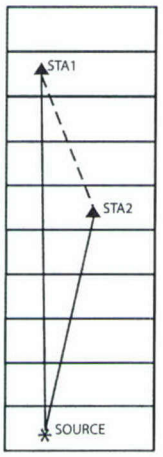

Figure 7-3. We assumed a 1-D profile for Q inversion. The dashed line is the great circle connecting stations 1 and 2. Inter-station Q is measured for the dashed line path. All possible two-station pairs are used for the inversion.

s_{mn} is the area where the nth path overlaps with the m^{th} grid, S_n is the total cells for each path, Q_m^i is a starting model for m being m=1,2,3,…,N_g (Figure 7-3). For each of the m grids (m=1,2,3,…,N_g), a new estimate of Q_m, denoted by Q_m^{i+1}, is made by back projecting Δ_n^i into the inverse of the Q_m^i's

$$\frac{1}{Q_m^{i+1}} = \frac{1}{Q_m} + \frac{1}{N_i} \sum_{n=1}^{N_d} \frac{\Delta_n^i s_{mn}}{\sum_{j=1}^{N_g} s_{jn}^2} \qquad (7.11)$$

To stabilize the convergence and smooth the model Suetsugu and Nakanishi (1985) proposed a nine point spatial smoothing procedure (Xie and Mitchell, 1990, Equation 14). We used less smoothing points then the original method since we are only resolving 1D variation.

7.6 ERROR ANALYSIS.

The error analysis can be approximated using standard deviation of each single trace Q measurements. It is assumed that this σ_Q gives a measure of the absolute value of statistical error (Xie and Mitchell, 1990). The error values are empirically constructed using the mean of σ_Q. This mean value is used to generate Gaussian random noise series whose number is $20xN_g$. The number of generated noise series are then added to Q_n,

$$Q_n^{'} = Q_n + \delta Q_n \qquad (7.12)$$

These $Q^{`}_n$ values are inverted 20 times and compared with original Q_m image. The difference gives the amount of error in coda Q estimate.

Back projection tomography does not yield a resolution matrix. Xie and Mitchell (1990) used a technique that is based on an approximation to the resolution kernel. By reconstructing the chosen block with a unit value, we can estimate the amount of model produced by a unit-valued Q^{-1} at the geographic point of interest. This technique is called as point spreading function (psf) and the rest of the model other than unity is assigned to zero. The synthetic data is used as an input model and inverted via backprojection to estimate the spreading of a unit grid.

For the analysis of lateral variation in Tibet, we first found a profile which best fits the station points using least squares. Then, we transformed the spherical coordinates to Cartesian coordinates and rotated using the Euler pole rotation. The purpose is to eliminate the errors caused by the sphericity of the earth. The new station coordinate arranged to lie along the equatorial latitude. The two-station pairs for each array (INDEPTH-II and INDEPTH-III) were arranged across the profile so that they do not oversample one point and moving with the same separation. The profiles were inverted using a 0.1 degree cell size.

7.7 RESULTS.

The INDEPTH II profile is located in Southern Tibet where partially molten middle crust exists north of the Kangmar dome, about 80 km south of the IYS, to central Tibet (e.g. Nelson et al., 1996; Kind et al., 1996). We used both Spectral Inversion and Two-Station methods allowing comparing the results obtained from different estimates of *Lg* Q_0.

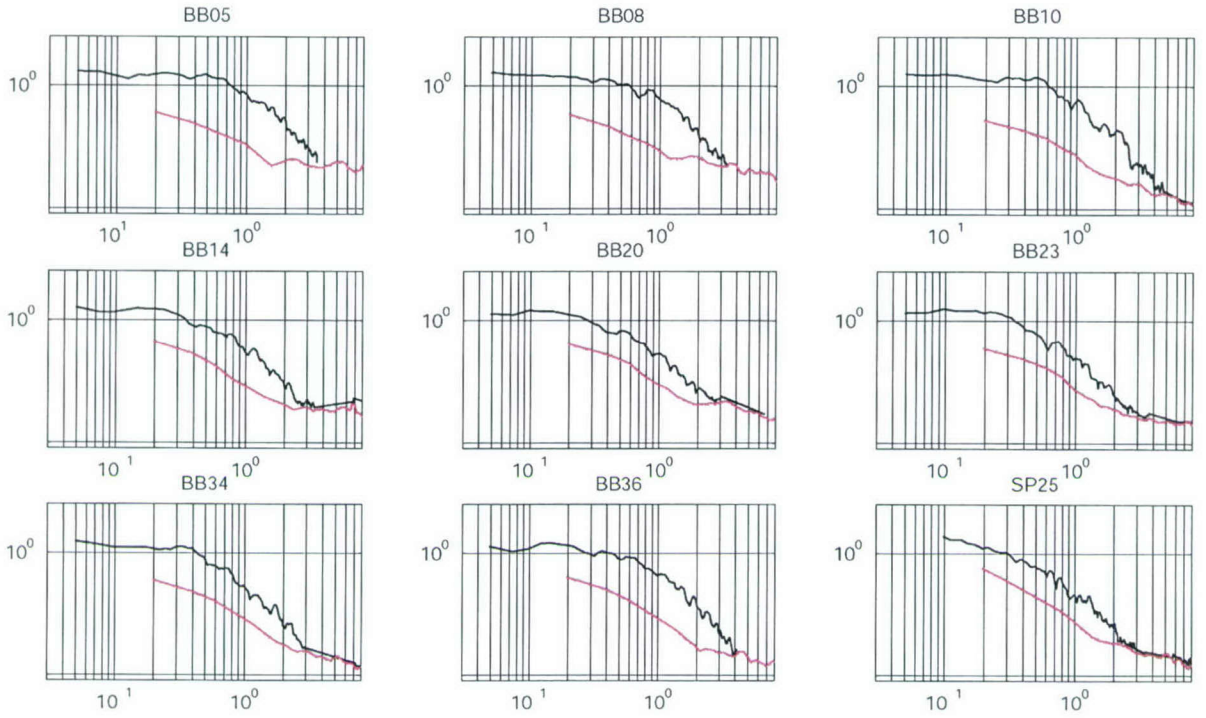

Figure 7-4. Example of displacement spectra with the noise window from INDEPTH II. Event 1994 236 21:08 Mb=5.5. Distance to first station BB05 is about 350 km.

To perform the spectral inversion on the stations in Figure 7-1, we first calculated the displacement spectra of each station and removed the effect of noise and geometrical spreading (Figures 7-2 and 7-4). Spectra with a good S/N ratio are selected for inversion. The frequency range in the inversion is adjusted to minimize the noise contribution. The selected spectra are used for the inversion after a couple of successive iterations that are narrowed around the solution. We select the solution with the minimum residual (Equation 7.5). Since our main concern is the attenuation of Lg, we did not include M_o and f_c on the map, though they are given in Table 7-1. Figure 7-5 shows the result of *Lg* Q_0 at Southern Tibet.

It is notable to see the higher attenuation at the north of the Kangmar dome. Because Sn propagation is efficient from nearby earthquakes originated in the Indian Shield and the Himalayas (Ni and Barazangi, 1983; McNamara, 1996) and the coda of Sn will contaminate the Lg phase, thus these nearby southern events are not used in this study. The significant difference for *Lg* Q_0 is for the event occurred in Indian Shield with Lg Q_0 =225. Such a low Q value is clearly not a true representation of the Indian Shield; rather it is a measure of attenuation through the Indian Shield, Himalayas and Southern Tibet.

Table 7-1. Spectral inversion results of INDEPTH II.

Date(yyjdy)	O.Time	Q_0	η(eta)	Mo(dyne-cm)	fc(hz)
94160	22:53	136	0.7	$1.2x10^{23}$	1.3
94176	08:32	110	0.8	$9 x10^{22}$	0.6
94180	18:22	112	0.5	$7 x10^{24}$	0.4
94181	00:48	86	0.7	$1.4 x10^{24}$	0.4
94204	20:57	74	0.7	$4.3 x10^{24}$	0.7
94205	23:39	180	0.5	$1.1 x10^{23}$	0.9
94216	05:08	70	0.8	$9 x10^{22}$	0.5
94236	21:08	116	0.3	$1.1 x10^{23}$	1.3
94237	16:47	90	0.6	$6 x10^{22}$	0.6
94243	23:29	225	0.7	$2.6 x10^{23}$	1.3

Two-station *Lg* Q_0 results are shown in Figure 7-6. We used these inter-station Q values to measure lateral changes along the profile. Since the INDEPTH II experiment was operated about six months it is hard to find many events aligned along the same great circle path. We used one event (1994 08/24(236) 21:08:47.3 Mb=5.5), which occurred north of the array (Figure 7-7). Although the station separation should normally be kept longer than 150-200 km, we used even shorter distances. The fact is that dramatically high attenuation allows us to use short station separation. The same data preparation as for spectral inversion is applied to waveforms such as removal of geometrical spreading and noise effects. Each spectrum is then smoothed using 17-point running-average (Figure 7-8). Figure 7-9 shows the lateral variation of *Lg* Q_0 along the INDEPTH II profile. We observe very low attenuation areas just north of the IYS (~50-60). The slight increase of Q (~100) is well observed for the southernmost part of the INDEPTH-II array where is geographically known as the high Tethyan Himalayas.

Table 7-2. Spectral inversion results of INDEPTH III.

Date(yyjdy)	O.Time	Q_0	η(eta)	Mo(dyne-cm)	fc(hz)
98318	04:11	111	0.5	$2x10^{22}$	1.2
98331	06:32	87	0.4	$4x10^{22}$	1.7
98359	10:44	86	0.6	$6x10^{22}$	1.0
99068	10:09	155	0.3	$1x10^{23}$	0.4
99092	09:39	97	0.5	$9x10^{22}$	0.8
99149	20:10	108	0.4	$9.4 x10^{23}$	0.9

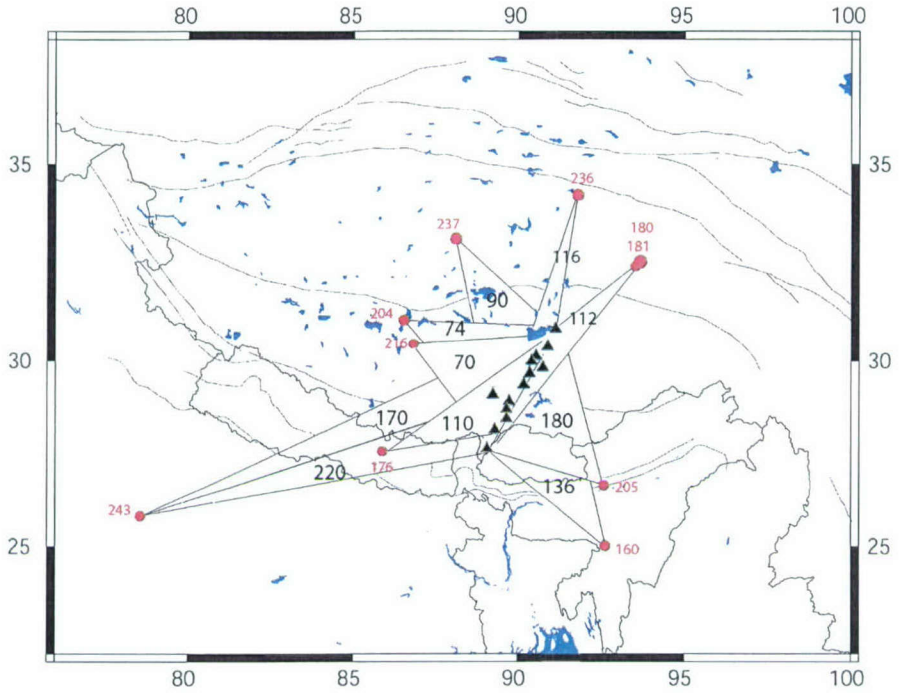

Figure 7-5. Spectral inversion results INDEPTH II. Red dots and indicate events, red numbers are Julian days. Lg Q_0 is given in shaded area.

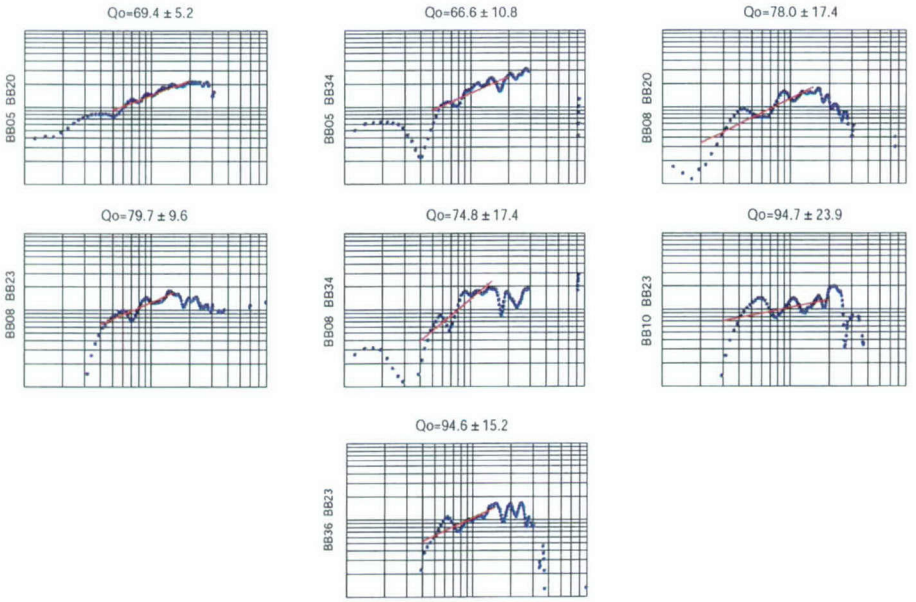

Figure 7-6. Station pairs calculated using 17 point smoothed spectra. Since the smoothing procedure will effect frequency dependence term we did not include at results.

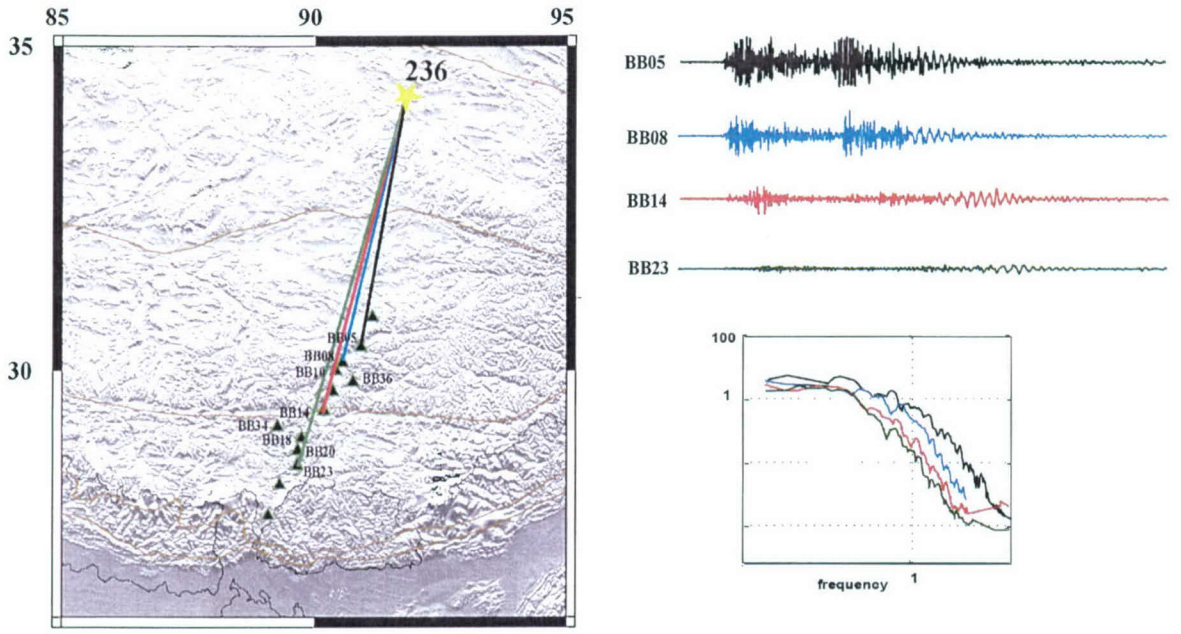

Figure 7-7. Location of event 1994 236 and examples of waveforms with their spectra. Note the significant attenuation/blockage of Lg for higher frequencies.

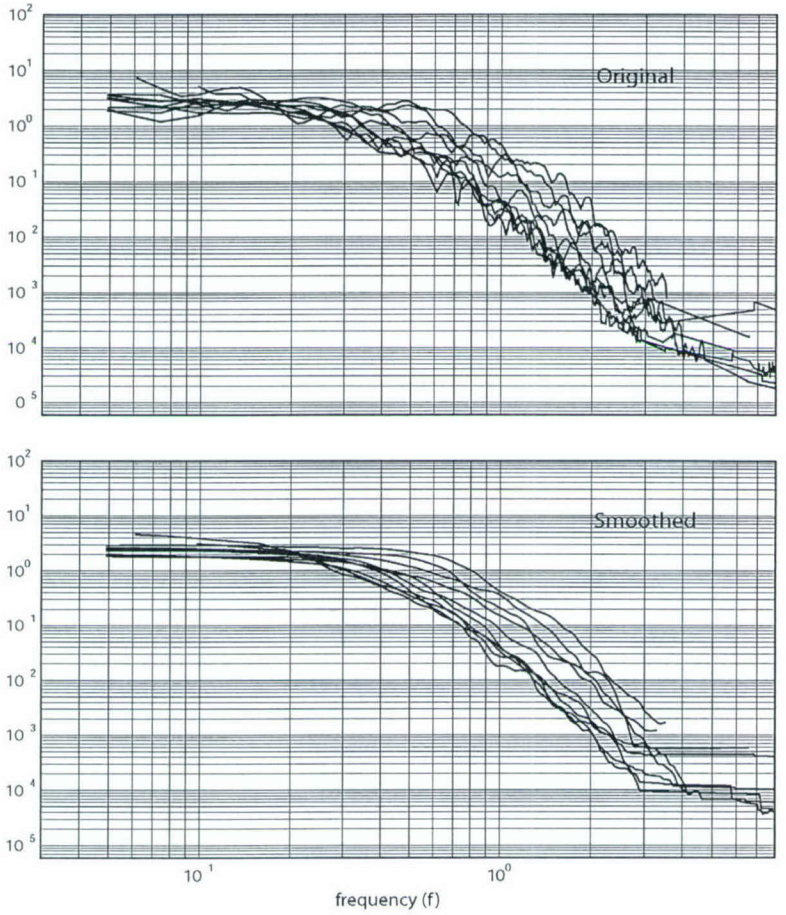

Figure 7-8. The 17 point smoothed spectra of event 1994 236 21:08.

INDEPTH III recorded along a NNW-SSE seismic profile in central Tibet (Figure 7-1) across the Banggong-Nujiang suture (BNS). During the period of one year some regional earthquakes were recorded. The dense distribution of stations allowed us to use both spectral inversion and two-station inversion methods, despite a number of quality events. Results are shown in Table 7-2.

We used all possible station pairs using a station separation of about 200 km (Figure 7-10). An event that occurred very close to the BNS allowed us to visually compare the characteristics of Lg traveling to Southern and Northern Tibet (Figure 7-11). No major differences in the spectra are observed. The two-station inversion result is shown in Figure 7-12. Apparently, using the two events along the same great circle path for two-station inversion gives similar results with no major change along the profile. To show the attenuation difference in central and Southern Tibet,

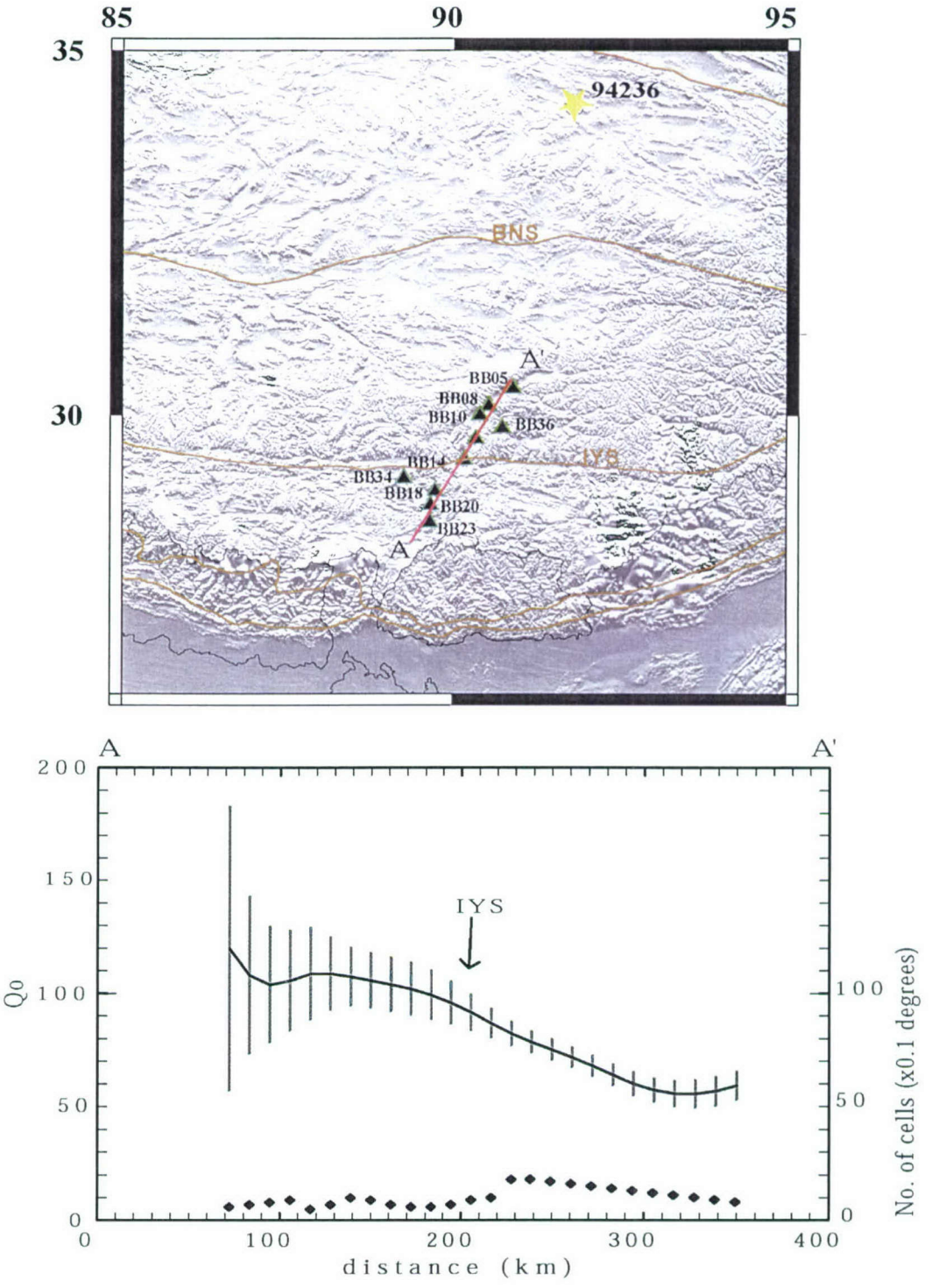

Figure 7-9. Lateral variation of Lg Q_0 through INDEPTH II profile. Green lines are error bars, black dots are the lateral resolution in units of cells.

we selected two events recorded along INDEPTH II and INDEPTH III arrays. The drastic change in both amplitude and frequency within the same distance is seen for INDEPTH II stations (Figure 7-13). This difference indicates the Southernmost Tibet where the mid-crust is molten has a large attenuation on the Lg phase.

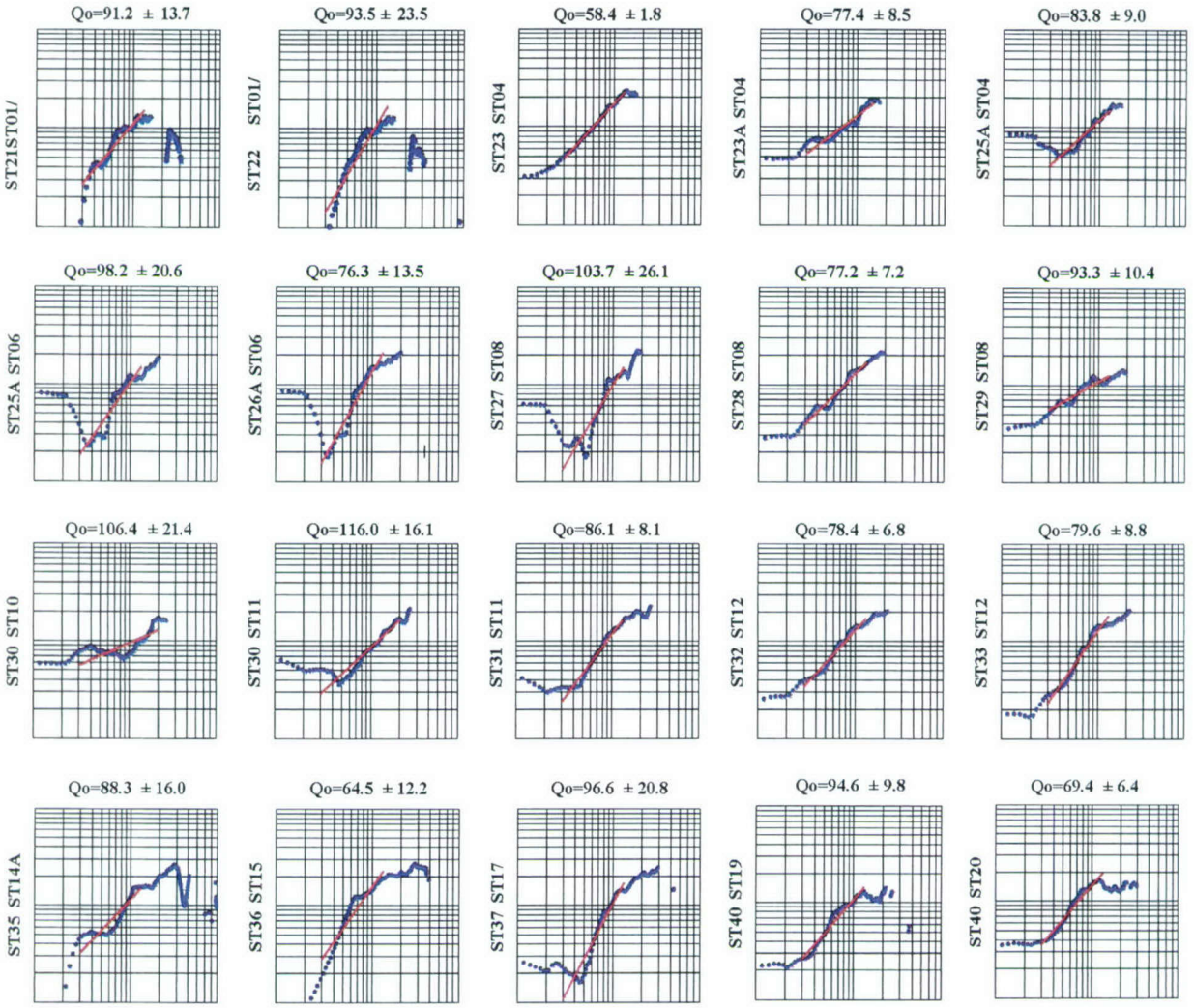

Figure 7-10. Two station pairs for INDEPTH III event 1998 331.

For paths crossing the Tibetan Plateau, *Lg* phase is not observed for paths longer than 600-700 km (McNamara et al., 1996). McNamara et al. analyzed data of this experiment for the presence of *Lg* as well as attenuation to each station using data collected by the 1991-1992 PASSCAL Tibet experiment. In order to cover a larger area, we included the *Lg* paths to INDEPTH II stations (Figures 7-14 and 7-15). Before selecting earthquakes for Lg attenuation we checked the presence of this phase at each station. The stations and events are shown in Figure 7-15, events and results are listed in Table 7-3.

We did not apply the two-station method for detailed lateral variation along the array because the station distribution is so sparse for such an application. However, Xie (2002) has used two-station pairs by averaging them for a small region and found *Lg* Q_0 =126 for a part of Eastern Tibetan plateau.

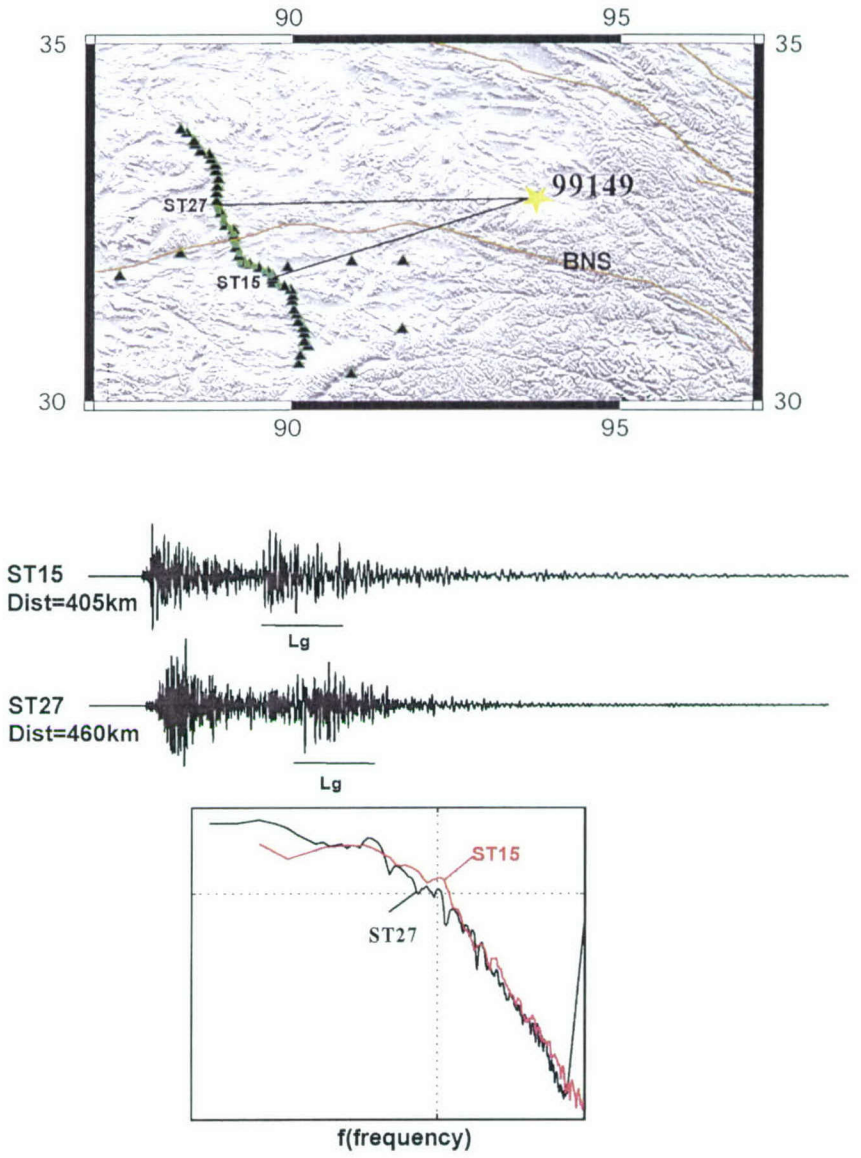

Figure 7-11. Comparison of two waveforms from south and north of suture. There is no significant change is observed.

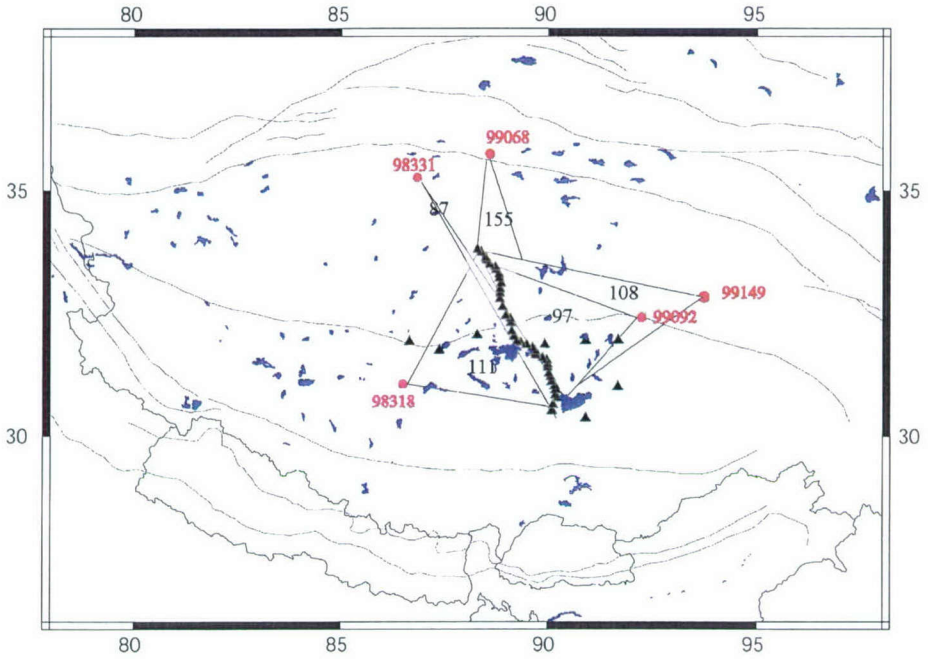

Figure 7-12. Station and events with Lg Q_0 values for INDEPTH III.

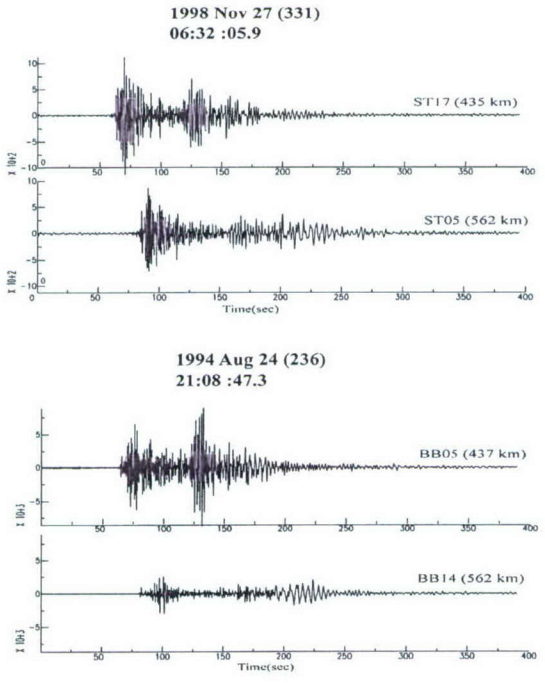

Figure 7-13. Comparison of attenuation for the same epicentral distances of INDEPTH II and INDEPTH III. Waveforms are bandpass filtered between 0.5-5 Hz. Distance to the event is given in parenthesis of each station name.

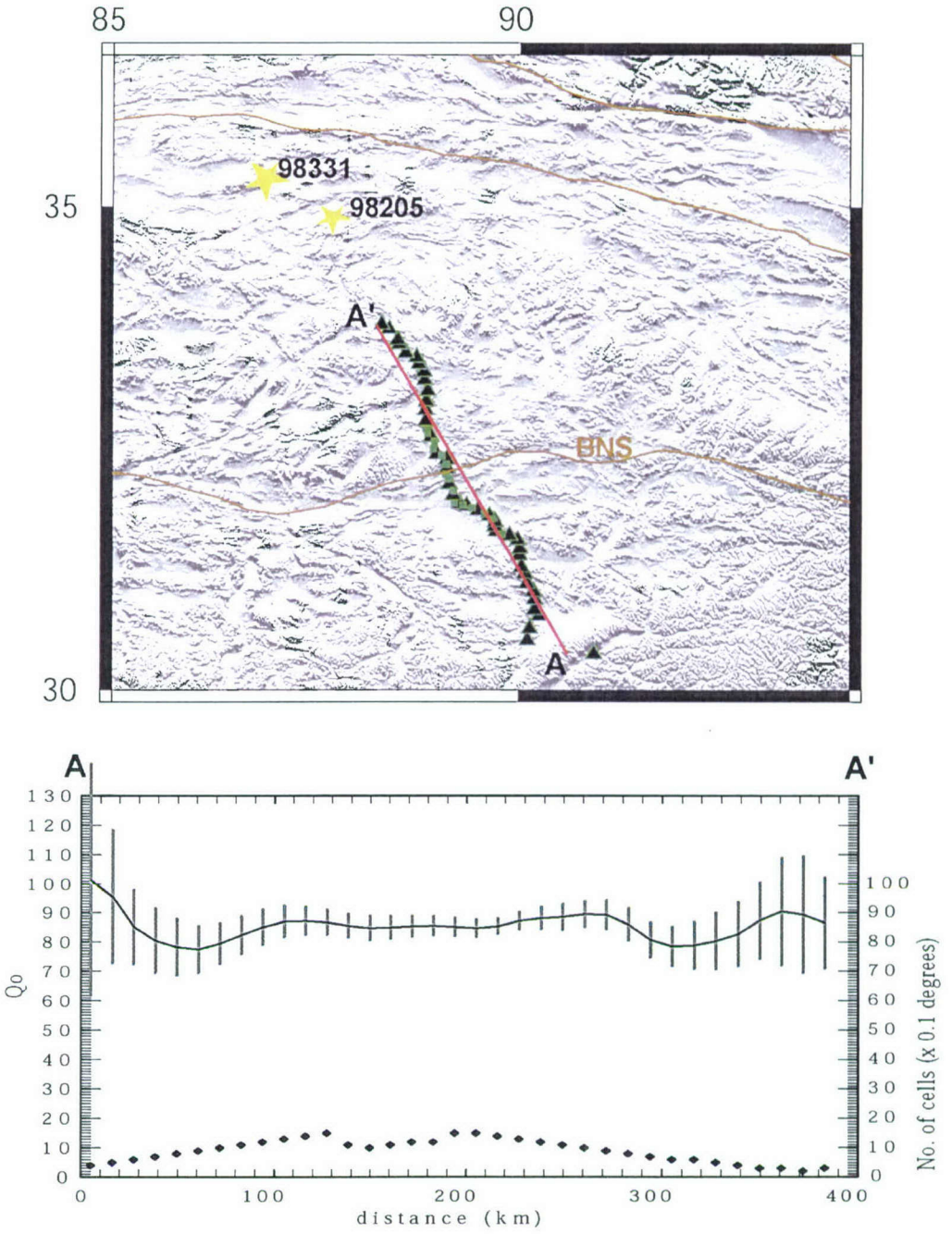

Figure 7-14. Two-station lateral variation inversion results for INDEPTH III. Green lines are error bars. Black dots at lower part of the plot shows lateral resolution in cells of 0.1 degrees distance.

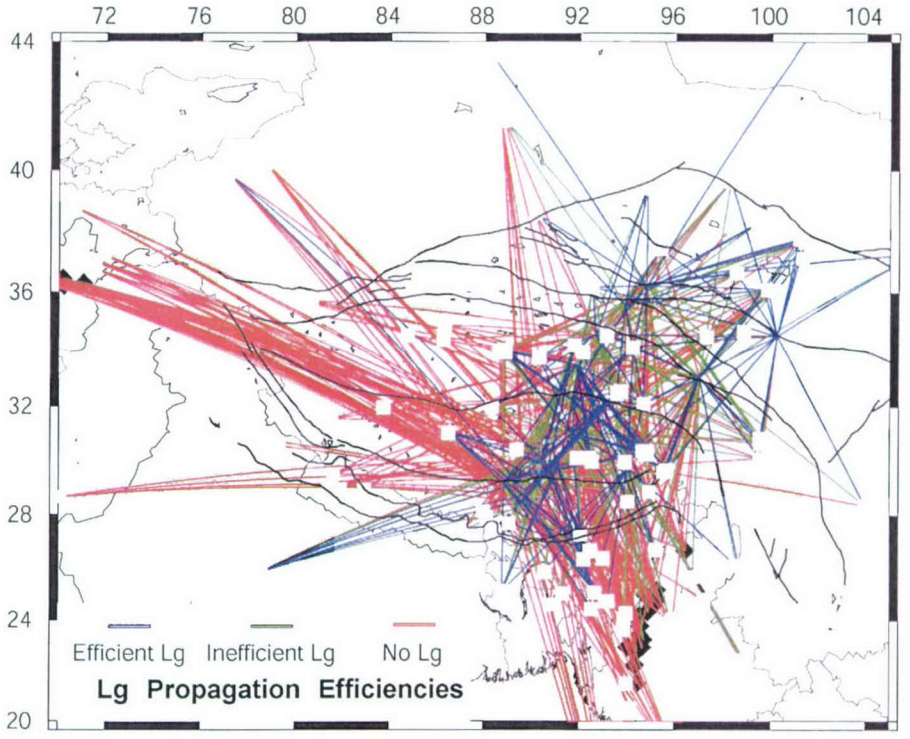

Figure 7-15. Lg propagation in Tibet using INDEPTH II and 1991-92 PASSCAL Experiment.

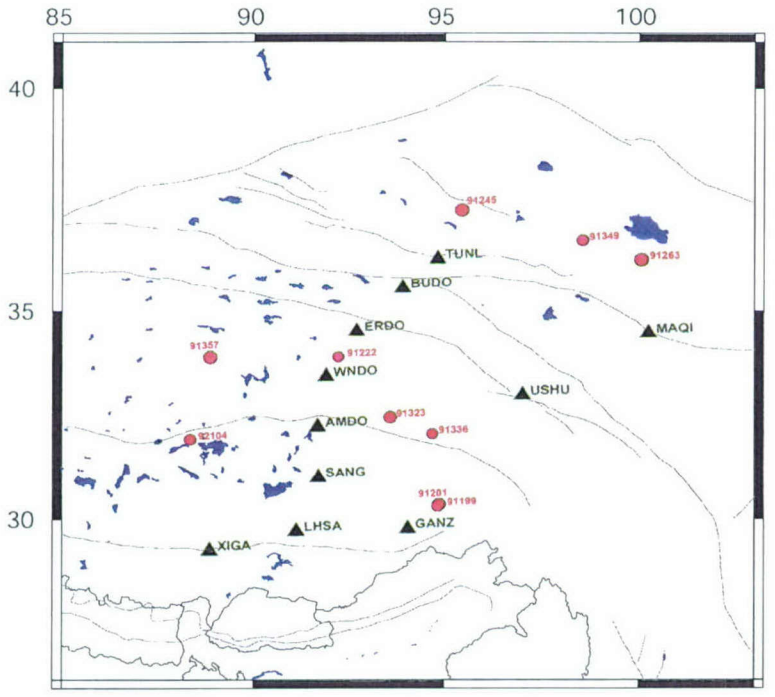

Figure 7-16. Stations and events used for spectral inversion of 1991-1992 PASSCAL Experiment.

Table 7-3. Spectral inversion results of 1991-1992 Tibet PASSCAL Experiment.

DATE(yyjdy)	O.Time	Q_0	η(eta)	Mo(dyne-cm)	fc(Hz)
91199	13:24	81	0.7	3.6×10^{23}	0.6
91201	19:02	107	0.6	6×10^{22}	0.7
91245	11:05	94	0.6	8×10^{23}	0.7
91251	23:54	83	0.7	1×10^{23}	2.4
91263	11:16	110	0.8	3×10^{24}	0.3
91323	1:04	84	0.7	2.8×10^{23}	0.5
91336	19:45	95	0.6	21×10^{23}	0.5
91349	15:59	81	0.7	6.2×10^{23}	0.6
91357	1:58	89	0.6	2.5×10^{23}	0.7
92104	3:47	123	0.5	9×10^{22}	0.6

7.8 CONCLUSIONS.

The high attenuation in the crust of Tibet was estimated using three different array dataset. The *Lg* Q_0 in the eastern part of Tibet is found about ~100-110 similar to the two-station inversion study of Xie (2002) (*Lg* Q_0 =126±9). In this study we found that there are regions of extremely high attenuating Lg in the southernmost of Tibet. It appears the high attenuation is intimately related to the mid-crustal partial melt. Fan and Lay (2002) found higher Lg Q using earthquakes that are more distant from station WMQ. They found *Lg* Q_0 =316 for the southern part of Tibet. Our *Lg* Q_0 estimates for Southernmost Tibet, using data collected within Tibet, are very low (60-100). The lowest attenuation is in the vicinity of IYS (~60) and higher for the area south of Kangmar dome (~100) (Figure 7-9). However, large error due to limited data, which sampling this complicated region, the location of the change of low to high attenuation in Southern Tibet cannot be resolved yet. Moreover, any major structure change at IYS that can cause large scattering is not resolved. We observe that INDEPTH III *Lg* Q_0 results are also about 80-110. There is apparently no large attenuation change in central to Southern Tibet. Data in Northern Tibet is limited and how the Lg attenuation behaves is not well known. Very low Q found in Tibet would explain the limiting distance of 600-700 km for observing *Lg* in Eastern and central part of Tibet. These values of Lg Q_0 may offer an alternative explanation for the *Lg* 'blockage' along the boundaries of the plateau. The low *Lg* Q_0 values are consistent with high temperature and presence of melt and fluid in the Tibetan crust. The lowest Q_0 in Southern Tibet is probably caused by a molten mid-crust. Attenuation values given above are very low for continental areas anywhere and can explain the high attenuation in Southernmost Tibet.

SECTION 8

REFERENCES

Akaike, H., Information theory and an extension of the maximum likelihood principle, in *Breakthroughs in Statistics, Vol. I, Foundations and Basic Theory*, S. Kotz and N.L. Johnson, eds, Springer-Verlag, New York, 1992, 610-624. (UNCLASSIFIED)

Annual Bulletin of Chinese Earthquakes, 1982-1995, China Seismological Bureau.

Bath, M., Propagation of Sn and Pn to teleseismic distances, *Geofis. Pura. Appl., 64, 19-30*, 1966. (UNCLASSIFIED)

Barazangi, M., and J. Ni, Velocities and propagation characteristics of Pn and Sn waves beneath the Himalayan Arc and Tibetan Plateau: Possible evidence for underthrusting of Indian continental lithosphere beneath Tibet, *Geology*, 10, 179-185, 1982. (UNCLASSIFIED)

Beghoul, N, M. Barazangi, B. Isacks, Lithospheric structure of Tibet and Western North-America: Mechanisms of uplift and a comparative study, *J. Geophys. Res.*, 98, 1997-2016, 1993. (UNCLASSIFIED)

Brune, J., and J. Dorman, Seismic waves and earth structure in the Canadian Shield, *Bull. Seism. Soc. Am. 53, 167-210*, 1963. (UNCLASSIFIED)

Bouchon, M., The complete synthesis of seismic crustal phases at regional distances, *J. Geophys. Res.*, 82, 1735-1741, 1982. (UNCLASSIFIED)

Campillo, M., Lg wave propagation in laterally varying crust and the distribution of the apparent quality factor in central France, *J. Geophys. Res., 92*, 12504-12514, 1987. (UNCLASSIFIED)

Chen, W., B. Burchfiel, Y. Liu, R. King, L. Royden, W. tang, E. Wang, J. Zhao, and X. Zhang, Global positioning system measurements from eastern Tibet and Their implications for India/Eurasia intercontinental deformation, *J. Geophys. Res.*, 105, 16215-16277, 2000. (UNCLASSIFIED)

Christensen, MI, and WD Mooney, Seismic velocity structure and composition of the continental crust: A global view, *J. Geophys. Res*, 100, 9761-9788, 1995. (UNCLASSIFIED)

Fan, G., and T. Lay, Characteristics of *Lg* attenuation in the Tibetan plateau, *J.Geophys. Res.*, submitted, 2002. (UNCLASSIFIED)

Gibson, R. L., and M. Campillo, Numerical simulation of high- and low-frequency Lg-wave propagation, *Geophys. J. Int., 118, 47-56*, 1994. (UNCLASSIFIED)

Guzman-Speziale, M, and J. F. Ni, The opening of the Andaman Sea: Where is the short-term displacement being taken up?, *Geophysical Research Letters*, 20, 2949 -2952, 1993. (UNCLASSIFIED)

Hearn, T., Uppermost mantle velocities and anisotropy beneath Europe, *J. Geophysical Research*, 104, 15,123-15,139, 1999. (UNCLASSIFIED)

Uppermost mantle velocities beneath China and surrounding regions Hearn, TM; Wang, SY; Ni, JF; Xu, ZH; Yu, YX; Zhang, XD Source: *J. Geophys. Res*, 109, B11301, 2004. (UNCLASSIFIED)

Holt, W., Correlated crust and mantle strain fields in Tibet, *Geology*, 28, 67-70, 2000. (UNCLASSIFIED)

Husebye, E. S., and B. O. Ruud, Wave propagation in a complex crust - CTBT implications, *Proceedings for the 18th Annual Seismic Research Symposium on Monitoring a Comprehensive Test Ban Treaty, Phillips Laboratory, 172-181*, 1996. (UNCLASSIFIED)

Kadinsky-Cade, K., M. Barazangi, J. Oliver, and B. Isacks, Lateral variations of high frequency seismic wave propagation at regional distances across the Turkish and Iranian Plateaus, *J. Geophys. Res., 86, 9377-9396*, 1981. (UNCLASSIFIED)

Kennett, B. L. N., Lg waves and structural boundaries, *Bull. Seism. Soc. Am.,* 76, 1113-1141, 1986. (UNCLASSIFIED)

Mayeda, K., Koyangi, S., Hoshiba, M., Aki, K., and Zeng, Y., A Comparative Study of Scattering, Intrinsic and Coda Q ½1 for Hawaii, Long Valley and Central California between 1.5 and 15 *Hz, J. Geophys. Res*., 97, 6643–6659, 1992. (UNCLASSIFIED)

McNamara, D. E., T. J. Owens, and W. R. Walter, Observations of regional phase propagation across the Tibetan Plateau, *J. Geophys. Res., 100, 22215-22229*, 1995. (UNCLASSIFIED)

McNamara, D. E., T. J. Owens, and W. R. Walter, Propagation characteristics of Lg across the Tibetan plateau, *Bull. Seism. Soc. Am.,* 86, 457-469, 1996. (UNCLASSIFIED)

McNamara D.E., Walter W.R., Owens T.J., Ammon C.J., Upper mantle velocity structure beneath the Tibetan Plateau from Pn travel time tomography, J. Geophysical Research, 102, 493-505, 1997. (UNCLASSIFIED)

McQuarrie, A., and C-L Tsai, *Regression and Time Series Model Selection*, World Scientific, 1998. (UNCLASSIFIED)

Michel, G., M. Becker, D. Anermann, C. Reigher, E. Reinhart and the GEOSSEA-Team, New evidence for crustal motion in E and SE Asia from GPS measurements, *Earth Planet. Sci. Let*., 187, 239-244, 2001. (UNCLASSIFIED)

Molnar, P., and J. Oliver, Lateral variations of attenuation in the upper mantle and discontinuities in the lithosphere. *J. Geophys. Res., 74, 2648-2682*, 1969. (UNCLASSIFIED)

Nelson, K. D., W. Zhao, L. D. Brown, J. Kuo, Jinkai Che, Xianwen Liu, S. L. Klemperer, Y. Makovsky, R. Meissner, J. Mechie, R. Kind, F. Wenzel, J. Ni, J. Nabelek, Chen Leshou, Handong Tan, Wenbo Wei, A. G. Jones, J. Booker, M. Unsworth, W. S. F. Kidd, M. Hauck, D. Alsdorf, A. Ross, M. Cogan, Changde Wu, E. Sandvol, and M. Edwards, Partially Molten Middle Crust Beneath Southern Tibet: Synthesis of Project INDEPTH Results, *Science*, 274, 1684-1687, 1996. (UNCLASSIFIED)

Ni, J., and M. Barazangi, High-frequency seismic wave propagation beneath the Indian Shield, Himalayan Arc, Tibetan Plateau and surrounding regions: high uppermost mantle velocities and efficient Sn propagation beneath Tibet, *Geophys. J. Roy. Astr. Soc.*, 72, 665-689, 1983. (UNCLASSIFIED)

Ni, J., and M. Barazangi, Velocities and propagation characteristics of Pn, Pg, Sn, and Lg seismic waves beneath the Indian Shield, Himalayan Arc, Tibetan Plat eau, and surrounding regions: High uppermost mantle velocities and efficient Sn propagation beneath Tibet, *Geophys. J. R. Astr. Soc.* 72, 665-689, 1984. (UNCLASSIFIED)

Nuttli, O.W., Seismic wave attenuation and magnitude relations for eastern North America, *J. Geophys. Res.*, 78, 5212-5218, 1973. (UNCLASSIFIED)

Oliver, J., M. Ewing, and F. Press, Crustal structure of the Arctic regions from the Lg phase, *Bull. Geol. Soc. Am., 66*, 1063-1074, 1955. (UNCLASSIFIED)

Press, F., and M. Ewing M., Two slow surface waves across North America, *Bull. Seism. Soc. Am., 42,* 219-228, 1952. (UNCLASSIFIED)

Rapine R., J. Ni, X. Wu, and T. Hearn, Regional wave propagation in China and surrounding regions, *Bull. Seism. Soc. Am.*, 87, 1,622-1,636, 1997. (UNCLASSIFIED)

Rapine, R., and J. Ni, Propagation characteristics of Sn and Lg in northeastern China and Mongolia, *Bull. Seism. Soc. Am.*, 93, 939-945, 2003. (UNCLASSIFIED)

Reese, C.C. and Ni, J., Attenuation of Coda Waves in Southern Tibet, *Geophys. Res. Let.*, 23, 3015-3018, 1996. (UNCLASSIFIED)

Ren, J., C. Jiang, Z. Zhang, D. Qin, Geotectonic Evolution of China, *Science Press, Beijing, 203*, 1987. (UNCLASSIFIED)

Rodgers, A., J. Ni, and T. Hearn, Pn, Sn, and Lg propagation in the Middle East, *Bull. Seism. Soc. Am., 87, 396-413*, 1997. (UNCLASSIFIED)

Royden LH, BC Burchfiel, RW King, E Wang, ZL Chen, F She and YP Liu, Surface deformation and lower crustal flow in eastern Tibet, *Science*, 276, 788-790, 1997. (UNCLASSIFIED)

Ruzaikin, A.I., I.L. Nersesov, V.I. Khalturin, and P. Molnar, Propagation of Lg and lateral variations of crustal structure in Asia, *J. Geophys. Res., 82*, 307-316, 1977. (UNCLASSIFIED)

Shen, F, LH Royden and BC Burchfiel, Large-scale crustal deformation of the Tibetan Plateau, *J. Geophys. Res*, 106, 6793-6816, 2001. (UNCLASSIFIED)

Suetsugu, D., and I. Nakanishi, Tomographic inversion and resolution for Rayleigh-wave phase velocities in the Pacific Ocean, J. Physics. Earth, 33 (4), 345-368, 1985. (UNCLASSIFIED)

Tapponnier P., Oblique stepwise growth of the Tibet Plateau, *Science*, 295, 277-277, 2002. (UNCLASSIFIED)

Tapponnier, P., and P. Molnar, Active Faulting and Tectonics in China, *J. Geophys. Res., 82*, 2905-2930, 1977. (UNCLASSIFIED)

Taylor, S. R., M. D. Denny, E. S. Vergino, and R. E. Glaser, Regional discrimination between NTS explosions and earthquakes, *Bull. Seism. Soc. Am., 79, 1142-1176*, 1989. (UNCLASSIFIED)

W-C Huang, J. F. Ni, F. Tilmann, D. Nelson, J. Guo, W. Zhao, J. Mechie, R. Kind, J. Saul, R. Rapine, and T. M. Hearn, Seismic polarization anisotropy beneath the central Tibetan Plateau, *Journal of Geophysical Research*, 105, 27979-27989, 2000. (UNCLASSIFIED)

Wu, J. P., R. S. Zeng, and Y. H. Ming, Upper mantle P wave velocity of the northern part of China and Mongolia, *Acta Seismologica Sinica, 11, 1-14*, 1998. (UNCLASSIFIED)

Xie, J., Simultaneous inversion of source spectra and path Q using Lg with applications to three Semipalatinsk explosions, *Bull. Seism. Soc. Am.*, 83, 1547-1562, 1993. (UNCLASSIFIED)

Xie, J., Spectral inversion using Lg from earthquakes: Improvement of the method with applications to the 1995, western Texas earthquake sequence, *Bull. Seism. Soc. Am.*, 88, 1525-1537, 1998 (UNCLASSIFIED)

Xie, J., Lg Q in the Eastern Tibetan Plateau, *Bull. Seism. Soc. Am*, 92, 871-876, 2002. (UNCLASSIFIED)

Xie, J. and B.J. Mitchell, Attenuation of multiphase surface waves in the Basin and Range province, Part 1: Lg and Lg coda. *Geophysical Journal*, 102, 121-138, 1990. (UNCLASSIFIED)

Yang, X. and C. Romney, *PIDC ground truth event (GT) database*, CMR Technical Report 99-15, 1999. (UNCLASSIFIED)

Yin A, Harrison T. M, Geologic evolution of the Himalayan-Tibetan orogen, *Annual Review of Earth and Planetary Sciences*, 28, 211-280, 2000. (UNCLASSIFIED)

Yin, A., Nei, S., A Phanerozoic palinspastic reconstruction of China and its neighboring regions, in *The Tectonic Evolution of Asia*, Cambridge University Press, 442-485, 1996. (UNCLASSIFIED)

DISTRIBUTION LIST
DTRA-02-13

DEPARTMENT OF DEFENSE

DIRECTOR
DEFENSE INTELLIGENCE AGENCY
BUILDING 6000
WASHINGTON, DC 20340-5100
ATTN: DTIB

DIRECTOR
DEFENSE RESEARCH AND ENGINEERING
3030 DEFENSE PENTAGON
WASHINGTON, D.C. 20301-3030
ATTN: DDR&E, ROOM 3E808

DEFENSE TECHNICAL INFORMATION CENTER
8725 JOHN J. KINGMAN ROAD, SUITE 0944
FT. BELVOIR, VA 22060-6218
ATTN: DTIC/OCA

DEFENSE THREAT REDUCTION AGENCY
8725 JOHN J. KINGMAN ROAD MS 6201
FT. BELVOIR, VA 22060-6201
ATTN: TDND, CPT. BARBER

OFFICE OF THE SECRETARY OF DEFENSE
CHEMICAL DEMILITARIZATION AND THREAT
REDUCTION OFFICE
1515 WILSON BOULEVARD, SUITE 720
ARLINGTON, VA 22209-2402
ATTN: P. WAKEFIELD
ATTN: DR. S. MANGINO

DEPARTMENT OF THE ARMY

US ARMY SMDC
SMDC-TC-YD
P.O. BOX 1500
HUNTSVILLE, AL 35807 3801
ATTN: B. ANDRE

DEPARTMENT OF THE AIR FORCE

AIR FORCE RESEARCH LABORATORY
29 RANDOLPH ROAD
HANSCOM AFB, MA 01731
ATTN: RESEARCH LIBRARY
ATTN: VSBL, R. RAISTRICK

USAF AT USGS
2201 SUNRISE VALLEY DRIVE MS 951
RESTON, VA 20192
ATTN: R. BLANDFORD
ATTN: R. JIH

AIR FORCE TECHNICAL APPLICATIONS CTR
1030 S. HIGHWAY AIA
PATRICK AFB, FL 32925 3002
ATTN: CA/STINFO
ATTN: TTR, D. CLAUTER

ATTN: CTI, DR. B. KEMERAIT
ATTN: TT, DR. D. RUSSELL
ATTN: TTR, F. SCHULTZ
ATTN: TTR, G. ROTHE
ATTN: TTR, V. HSU
ATTN: DR. B. NGUYEN
ATTN: DR. E. SMART
ATTN: DR. G. WAGNER
ATTN: DR. M. WOODS

DEPARTMENT OF THE NAVY

NAVAL RESEARCH LABORATORY
4555 OVERLOOK AVE, SW, CODE 7643
WASHINGTON, DC 20375 0001
ATTN: DR. D. DROB

DEPARTMENT OF ENERGY

NATIONAL NUCLEAR SECURITY
ADMINISTRATION
1000 INDEPENDENCE AVE SW
WASHINGTON, DC 20585 0420
ATTN: L. CASEY
ATTN: G. KIERNAN

UNIVERSITY OF CALIFORNIA
LAWRENCE LIVERMORE NATIONAL LAB
P.O. BOX 808
LIVERMORE, CA 94551 9900
ATTN: MS L205, DR. D. HARRIS
ATTN: MS 205, TECHNICAL STAFF

LOS ALAMOS NATIONAL LABORATORY
P.O. BOX 1663
LOS ALAMOS, NM 87545
ATTN: MS C335, DR. S. R. TAYLOR

PACIFIC NORTHWEST NATIONAL LABORATORY
P.O. BOX 999
1 BATTELEE BOULEVARD
RICHLAND, WA 99352
ATTN: MS P8-20, T. HEIMBIGNER
ATTN: MS K8-29, DR. N. WOGMAN

SANDIA NATIONAL LABORATAORIES
MAIL SERVICES
P.O. BOX 5800
ALBUQUERQUE, NM 87185 1164
ATTN: WILLIAM GUYTON

OTHER GOVERNMENT

DEPARTMENT OF STATE
2201 C STREET NW
WASHINGTON, DC 20520
ATTN: R. MORROW, ROOM 5741

US GEOLOGICAL SURVEY
905 NATION CENTER
12201 SUNRISE VALLEY DR
RESTON, VA 20192
ATTN: W. LEITH

US GEOLOGICAL SURVEY
345 MIDDLEFIELD RD MS 977
MENLO PARK, CA 94025
ATTN: S. DETWEILER
ATTN: DR. W. MOONEY

DEPARTMENT OF DEFENSE CONTRACTORS

BATTELLE
MANAGER, ENERGETIC SYSTEMS & SECURITY TECHNOLOGIES
505 KING AVE
COLUMBUS, OH 43201-2693
ATTN: NEAL OWENS (7-2-081)

BBN CORPORATION
1300 N 17TH STREET, SUITE 400
ARLINGTON, VA 22209
ATTN: DR. D. NORRIS
ATTN: R. GIBSON
ATTN: J. PULLI

CENTER FOR MONITORING RESEARCH
1953 GALLOWS ROAD, SUITE 260
VIENNA, VA 22182 3997
ATTN: DR. K. L. MCLAUGLHLIN
ATTN: DR. R. WOODWARD
ATTN: DR. R. NORTH
ATTN: DR. X. YANG
ATTN: LIBRARIAN

ENSCO, INC.
5400 PORT ROYAL ROAD
SPRINGFIELD, VA 22151 2312
ATTN: D. BAUMGARDT
ATTN: Z. DER

WESTON GEOPHYSICAL CORPORATION
27 BEDFORD ST, SUITE 102
LEXINGTON, MA 02420
ATTN: DR. D. REITER
ATTN: J. LEWKOWICZ
ATTN: DR. A. ROSCA
ATTN: DR. I. TIBULEAC
ATTN: M. JOHNSON

ITT INDUSTRIES
ITT SYSTEMS CORPORATION
1680 TEXAS STREET SE

KIRTLAND AFB, NM 87117 5669
2 CYS ATTN: DTRIAC
ATTN: DARE

JAYCOR
1900 CAMPUS COMMONS DR SUITE 600 RESTON,
VA 20191-1535
ATTN: DR. C. P. KNOWLES

MISSION RESEARCH CORPORATION
8560 CINDERBED ROAD, SUITE 700
NEWINGTON, VA 22122
ATTN: DR. M. FISK

MULTIMAX, INC
1441 MC CORMICK DRIVE
LANDOVER, MD 20785
ATTN: DR. I. N. GUPTA
ATTN: W. RIVERS

MULTIMAX, INC
1090 N HIGHWAY A1A SUITE D
INDIANLATIC, FL 32903
ATTN: DR. H. GHALIB

SCIENCE APPLICATIONS INTERNATIONAL CORP
10260 CAMPUS POINT DRIVE
SAN DIEGO, CA 92121 1578
ATTN: DR.M. ENEVA
ATTN: DR. G. E. BAKER
ATTN: DR. J. STEVENS
ATTN: DR. D. ADAMS

SCIENCE APPLICATIONS INT'L CORP
1227 S. PATRICK DR SUITE 110
SATELLITE BEACH, FL 32937
ATTN: DR. M. FELIX
ATTN: DR. H. GIVEN

URS CORPORATION
566 EL DORADO STREET
PASADENA, CA 91109 3245
ATTN: DR. N.B. WOODS
ATTN: DR. C. SAIKIA
ATTN: DR. G. ICHINOSE

DIRECTORY OF OTHER (LIBRARIES AND UNIVERSITIES)

BOSTON COLLEGE
INSTITUTE FOR SPACE RESEARCH
140 COMMONWEALTH AVENUE
CHESTNUT HILL, MA 02167
ATTN: DR. D. HARKRIDER
ATTN: B. SULLIVAN

BROWN UNIVERSITY
DEPARTMENT OF GEOLOGICAL SCIENCES
75 WATERMAN STREET
PROVIDENCE, RI 02912 1846
ATTN: PROF. D. FORSYTH

CALIFORNIA INSTITUTE OF TECHNOLOGY
DIVISION OF GEOLOGY & PLANETARY SCIENCES
PASADENA, CA 91125
ATTN: PROF. DONALD V. HELMBERGER
ATTN: PROF. THOMAS AHRENS

UNIVERSITY OF CALIFORNIA BERKELEY
281 MCCONE HALL
BERKELEY, CA 94720 2599
ATTN: PROF. B. ROMANOWICZ
ATTN: DR. D. DREGER

UNIVERSITY OF CALIFORNIA-DAVIS
DEPT OF STATISTICS
DAVIS, CA 95616
ATTN: R.H. SHUMWAY, DIV

STATISTICS

UNIVERSITY OF CALIFORNIA SAN DIEGO
SCRIPPS INSTITUTION OF TECHNOLOGY
9500 GILMAN DRIVE
LA JOLLA, CA 92093 0225
ATTN: DR. L. DEGROOT - HEDLIN
ATTN: DR. M. HEDLIN
ATTN: PROF. F. VERNON
ATTN: PROF. J. BERGER
ATTN: J. ORCUTT

UNIVERSITY OF CALIFORNIA SANTA CRUZ
INSTITUTE OF TECTONICS
SANTA CRUZ, CA 95064
ATTN: DR. R. S. WU
ATTN: PROF. T. LAY

UNIVERSITY OF COLORADO BOULDER
DEPT OF PHYSICS, CAMPUS BOX 390
BOULDER, CO 80309
ATTN: DR.R. ENGDAHL
ATTN: M. RITZWOLLER
ATTN: PROF. C. ARCHAMBEAU

COLUMBIA UNIVERSITY
LAMONT DOHERTY EARTH OBSERVATORY
PALISADES, NY 10964
ATTN: DR. J. XIE
ATTN: DR. W. Y. KIM
ATTN: PROF. P.G. RICHARDS
ATTN: DR. M. TOLSTOY

UNIVERSITY OF CONNECTICUT
DEPARTMENT OF GEOLOGY & GEOPHYSICS
STOORS, CT 06269 2045
ATTN: PROF. V.F. CORMIER, U-45,
ROOM 207

CORNELL UNIVERSITY
DEPARTMENT OF GEOLOGICAL SCIENCES
3126 SNEE HALL
ITHACA, NY 14853
ATTN: PROF. M.A. BARAZANGI

HARVARD UNIVERSITY
HOFFMAN LABORATORY
20 OXFORD STREET
CAMBRIDGE, MA 02138
ATTN: PROF. A. DZIEWONSKI
ATTN: PROF. G. EKSTROM

INDIANA UNIVERSITY
DEPARTMENT OF GEOLOGICAL SCIENCES
1005 10TH STREET
BLOOMINGTON, IN 47405
ATTN: PROF. G. PAVLIS

IRIS
1200 NEW YORK AVENUE, NW SUITE 800
WASHINGTON, DC 20005
ATTN: DR. D. SIMPSON

IRIS
1408 NE 45TH ST #201
SEATTLE, WA 98105
ATTN: DR. T. AHERN

MASSACHUSETTS INSTITUTE OF TECHNOLOGY
EARTH RESOURCES LABORATORY
42 CARLETON STREET
CAMBRIDGE, MA 02142
ATTN: DR. W. RODI
ATTN: PROF. M.N. TOKSOZ

MICHIGAN STATE UNIVERSITY LIBRARY
450 ADMINISTRATION BUILDING
EAST LANSING, MI 48824
ATTN: K. FUJITA

NEW MEXICO STATE UNIVERSITY
DEPARTMENT OF PHYSICS
LAS CRUCES, NM 88003
ATTN: PROF. J. NI
ATTN: PROF. T. HEARN

NORTHWESTERN UNIVERSITY
DEPARTMENT OF GEOLOGICAL SCIENCES
1847 SHERIDAN RD
EVANSTON, IL 60208
ATTN: PROF. E. OKAL

PENNSYLVANIA STATE UNIVERSITY
GEOSCIENCES DEPARTMENT
403 DEIKE BUILDING
UNIVERSITY PARK, PA 16802
ATTN: PROF. C. AMMON
ATTN: PROF. S. ALEXANDER
ATTN: DR. A. NYBLADE

SAN DIEGO STATE UNIVERSITY
DEPARTMENT OF GEOLOGICAL SCIENCES
SAN DIEGO, CA 92182
ATTN: PROF. S. M. DAY

SOUTHERN METHODIST UNIVERSITY
DEPARTMENT OF GEOLOGICAL SCIENCES
P.O. BOX 750395
DALLAS, TX 75275
ATTN: B. STUMP
ATTN: E. HERRIN
ATTN: P. GOLDEN

UNIVERSITY OF HAWAII- MANOA
P.O. BOX 1599
KAILUA-KONA, HI 96745 1599
ATTN: DR. M. A. GARCES

UNIVERSITY OF MISSISSIPPI
1 COLISEUM DRIVE
UNIVERSITY, MS 38677
ATTN: PROF. H. BASS

UNIVERSITY OF SOUTHERN CALIFORNIA
520 SEAVER SCIENCE CENTER
UNIVERSITY PARK
LOS ANGELES, CA 90089 0483
ATTN: PROF. C. G. SAMMIS
ATTN: PROF. T. JORDAN

UNIVERSITY OF WISCONSIN MADISON
1215 W DAYTON ST
MADSION, WI 53706 1600
ATTN: DR. C. THURBER

ST LOUIS UNIVERSITY
EARTH & ATMOSPHERIC SCIENCES
STATION 3507 LACLEDE AVE
ST LOUIS, MO 63103
ATTN: PROF. B. J. MITCHELL
ATTN: PROF. R. HERRMAN

UNIVERSITY OF MEMPHIS
3904 CENTRAL AVE
MEMPHIS, TN 38152
ATTN: DR. J. PUJOL

UNIVERSITY OF MEMPHIS
3876 CENTRAL AVE
MEMPHIS, TN 38152
ATTN: DR. C. LANGSTON

UNIVERSITY OF TEXAS AUSTIN
IGS 130
AUSTIN, TX 78712
ATTN: DR. J. PULLIAM

UNIVERSITY OF TEXAS AUSTIN
IGS 131
AUSTIN, TX 78712
ATTN: DR. M. SEN

UNIVERSITY OF TEXAS EL PASO
DEPT OF GEOLOGICAL SCIENCES
EL PASO, TX 79901
ATTN: PROF. G. KELLER
ATTN: DR. D. DOSER
ATTN: DR. A. VELASCO

FOREIGN

AUSTRALIAN GEOLOGICAL SURVEY
ORGANIZATION
CORNER OF JERRAGOMRRRA &
NINDMARSH DRIVE
CANBERRA, ACT 2609
AUSTRALIA
ATTN: D. JESPOSN

GEOPHYSICAL INSTITUTE OF ISRAEL
POB 182
LOD, 7100 ISRAEL
ATTN: DR. Y. GITTERMAN
ATTN: DR. A. SHAPIRA

GEOLOGICAL SURVEY OF CANADA
7 OBSERVATORY CRESCENT
OTTAWA K1A 0Y3 ONT
CANADA
ATTN: C. WOODGOLD

I.R.I.G.M. B.P. 68
38402 ST. MARTIN D'HERES
CEDEX, FRANCE
ATTN: DR. M. BOUCHON

MINISTRY OF DEFENSE
PROCUREMENT EXEUTIVE
BLACKNESS, BRIMPTON
READING FG7-4RS ENGLAND
ATTN: DR. D. BOWERS

NTNF/NORSAR
P.O. BOX 51
N-2007 KJELLER, NORWAY
ATTN: DR. F. RINGDAL
ATTN: T. KVAERNA
ATTN: S. MYKKELTVEIT